Proteolysis of fibrillin-2 microfibrils is essential for normal skeletal development

Timothy J. Mead[a], Daniel R. Martin[a], Lauren W. Wang[a], Stuart A. Cain[b], Cagri Gulec[c], Elisabeth Cahill[a], Joseph Mauch[a], Dieter P. Reinhardt[d], Cecilia W. Lo[c], Clair Baldock[b], Suneel S. Apte[a1]

[a]Department of Biomedical Engineering and Musculoskeletal Research Center, Cleveland Clinic Lerner Research Institute, Cleveland, OH 44195; [b]Division of Cell-Matrix Biology and Regenerative Medicine, Wellcome Centre for Cell-Matrix Research, School of Biological Sciences, Faculty of Biology, Medicine and Health, The University of Manchester, Manchester Academic Health Science Centre, Manchester, UK; [c]Department of Developmental Biology, University of Pittsburgh School of Medicine, Pittsburgh, PA 15201, [d]Department of Anatomy and Cell Biology and Faculty of Dentistry, McGill University, Montreal, Quebec, Canada.

Short title: ADAMTS proteostasis of microfibrils

[1]To whom correspondence should be addressed: Suneel S. Apte, MBBS, D.Phil., Department of Biomedical Engineering-ND20, Lerner Research Institute, Cleveland Clinic, 9500 Euclid Avenue, Cleveland, OH 44195, USA. Phone: 216.445.3278; E-mail: aptes@ccf.org

***Classification*:** BIOLOGICAL SCIENCES – Developmental Biology (or Cell Biology)

Key words: ADAMTS, metalloproteinase, limb development, skeletal development, extracellular matrix, microfibrils, fibrillin, Marfan syndrome, Weill-Marchesani syndrome.

Abstract:

The extracellular matrix (ECM) undergoes an orchestrated transition from embryonic to mature ECM that is essential for postnatal life, yet the developmental transition mechanisms for ECM components and macromolecular complexes are poorly defined. Fibrillin microfibrils are macromolecular ECM complexes with important structural and regulatory roles. In mice, *Fbn1* and *Fbn2* mRNAs, which encode the major microfibrillar components, are strongly expressed during embryogenesis. *Fbn2* mRNA levels rapidly decline postnatally, consistent with fibrillin-1 being the major component of adult tissue microfibrils. Here, by combining transgenic and N-terminomics strategies with in vitro analysis of microfibril assembly and intermolecular interactions, we identify cooperative proteolysis of fibrillin-2 by the secreted metalloproteases ADAMTS6 and ADAMTS10 as a mechanism contributing to postnatal fibrillin-1 dominance. The primacy of the protease-substrate relationship between ADAMTS6 and fibrillin-2 was unequivocally established by demonstrating a dramatic reversal of skeletal defects in *Adamts6*$^{-/-}$ embryos by *Fbn2* haploinsufficiency.

Introduction:

In addition to proliferation and differentiation of resident cells, proper tissue and organ structure and function depends on the extracellular matrix (ECM). How ECM architecture and stoichiometry is maintained and constantly adjusted through the dynamic events of morphogenesis and transition into the adult organism is unknown. Ontogenetically, the earliest cell collectives formed sheets and tubes with a well-established basement membrane that provided a substrate for cell migration and adhesive inputs that determined cell polarity. Gene duplication and other modifications of a core set of ECM-encoding genes allowed formation of a complex interstitial matrix that promoted evolution of ever more complex organisms (Huxley-Jones, Robertson et al., 2007), but presented challenges for remodeling of the increasingly diverse ECM repertoire. The challenge appears to have been met by concomitant expansion of genes encoding secreted and cell-surface proteases (Huxley-Jones, Apte et al., 2005, Huxley-Jones, Clarke et al., 2007). For example, of the relatively recently discovered 19 ADAMTS proteases in mammals compared to only 2 in the fruitfly, the majority cleave ECM molecules (Dubail & Apte, 2015, Mead & Apte, 2018). Which specific ECM structures and molecules are targets of individual proteases, the temporal and spatial control of proteolysis, and prospective cooperation or antagonism between proteases are all poorly understood. The embryonic interstitial ECM is highly hydrated owing to abundant macromolecular hyaluronan (HA)-proteoglycan aggregates whereas fibrillar components, primarily collagens and elastin, dominate juvenile and adult ECM composition to provide structural resilience compatible with the greater mechanical demands imposed during postnatal life. Beyond structural roles, ECM mediates sequestration and regulated release of morphogens and growth factors (Ramirez, Caescu et al., 2018, Thomson, Singh et al., 2019), and ECM proteolysis can generate bioactive moieties, termed matrikines (Ricard-Blum & Vallet, 2019).

Fibrillin microfibrils have a crucial role in tissue development and homeostasis by providing mechanical stability and limited elasticity to tissues and/or regulating growth factors of the TGFβ

superfamily (Ramirez et al., 2018, Thomson et al., 2019), along with a key role in elastic fiber assembly (Kozel & Mecham, 2019, Shin & Yanagisawa, 2019). Fibrillins and the closely related latent TGFβ-binding proteins are large, cysteine-rich glycoproteins containing many epidermal growth factor (EGF)-like repeats. Of the three known mammalian fibrillin isoforms, fibrillin-2 and fibrillin-3 (in humans) are primarily expressed during embryogenesis (Sabatier, Miosge et al., 2011, Zhang, Apfelroth et al., 1994, Zhang, Hu et al., 1995). The gene encoding fibrillin-3 is inactivated in mice (Corson, Charbonneau et al., 2004), providing a simpler scenario than in humans for investigating developmental regulation of microfibril composition and the role of proteolytic turnover therein. Among numerous gene mutations affecting the skeleton (Yip, Chan et al., 2019), *FBN1* and *FBN2* mutations cause distinct dominantly inherited human connective tissue disorders, Marfan syndrome and congenital contractural arachnodactyly, respectively (Robinson, Arteaga-Solis et al., 2006). Despite overlapping features such as skeletal overgrowth and poor muscular development, each disorder has its distinct manifestations, indicating that fibrillin isoforms may contribute specific properties to microfibrils, have a tissue-specific function, or form distinct ECM networks. Severe cardiovascular manifestations, especially aortic root and ascending aorta aneurysms, which are potentially lethal, as well as ocular manifestations occur frequently in Marfan syndrome, but neither is typically associated with *FBN2* mutations (Robinson et al., 2006). In mice, *Fbn2* deficiency affects myogenesis and distal limb patterning, reflecting a role for fibrillin-2 in BMP regulation (Arteaga-Solis, Gayraud et al., 2001, Sengle, Carlberg et al., 2015). Fibrillin microfibrils may be homotypic or contain both fibrillin-1 and -2 (Charbonneau, Dzamba et al., 2003, Lin, Tiedemann et al., 2002, Marson, Rock et al., 2005), but since each fibrillin appears to have distinct roles in vivo as well as in vitro (Nistala, Lee-Arteaga et al., 2010), an intriguing question is how the correct stoichiometry of the two fibrillins is maintained, and what impact an excess of fibrillin microfibrils or altered fibrillin stoichiometry may have on biological systems. Here, analysis of mouse mutants of the highly homologous secreted metalloproteases ADAMTS6 and ADAMTS10 reveals their crucial role in maintenance of fibrillin microfibril

proteostasis and potentially, fibrillin isoform stoichiometry, and illustrates one mechanism by which ECM composition is regulated during skeletal development in preparation for postnatal life.

Recessive *ADAMTS10* mutations lead to an acromelic dysplasia, Weil-Marchesani syndrome 1 (WMS1) (Dagoneau, Benoist-Lasselin et al., 2004), whereas dominant *FBN1* mutations cause a similar disorder, WMS2 (Faivre, Gorlin et al., 2003), suggesting a functional relationship between ADAMTS10 and fibrillin-1 (Hubmacher & Apte, 2015, Karoulias, Taye et al., 2020). ADAMTS10 binds fibrillin-1 directly and has been shown to accelerate fibrillin-1 microfibril biogenesis in vitro, but to cleave fibrillin-1 inefficiently (Cain, Mularczyk et al., 2016, Kutz, Wang et al., 2011). Mice homozygous for a human WMS-causing mutation had impaired long bone growth and increased muscle mass along with reduced fibrillin-1 staining in skeletal muscle and persistence of fibrillin-2 microfibrils in skeletal muscle and the eye (Mularczyk, Singh et al., 2018b, Wang, Kutz et al., 2019). *Adamts10*$^{-/-}$ mice are smaller than wild type littermates, and also showed fibrillin-2 accumulation in the ocular zonule (Wang et al., 2019). ADAMTS10 undergoes inefficient processing by furin, a general prerequisite for activation of ADAMTS proteases. ADAMTS10 which was constitutively activated by optimizing its furin processing site, proteolytically processed fibrillin-2 (Wang et al., 2019). Thus, the small fraction of ADAMTS10 that is normally activated by furin has proteolytic activity against fibrillin-2, yet ADAMTS10 does not apparently constitute a significant enough proteolytic mechanism on its own to lead to widespread fibrillin-2 accumulation. ADAMTS6 is highly homologous to ADAMTS10, sharing the same domain structure and having a high sequence identity. Because of strong evidence that homologous ADAMTS proteases can cooperate in several physiological contexts where they are co-expressed (Dubail, Aramaki-Hattori et al., 2014, Enomoto, 2010, McCulloch, Nelson et al., 2009, Mead, McCulloch et al., 2018b, Nandadasa, Kraft et al., 2019, Nandadasa, Nelson et al., 2015), we asked i) whether ADAMTS6 overlapped functionally with ADAMTS10 by investigating the impact of single or combined inactivation of *Adamts6* and *Adamts10* on mouse skeletal development, and ii) whether they

share the same proteolytic target. The findings are relevant to the role of ADAMTS10 in Weill-Marchesani syndrome and provide intriguing new insights into fibrillin microfibril proteostasis.

Results

Severe skeletal malformations in Adamts6-deficient mice are exacerbated by combined inactivation of Adamts10

Previous work had suggested that knockdown of ADAMTS6 or ADAMTS10 in cultured cells affected the expression level of the other (Cain et al., 2016). To investigate the possibility that germline inactivation of either mouse gene affected expression of the other, *Adamts6* and *Adamts10* mRNA levels were measured in limbs, heart and lungs of *Adamts6*$^{-/-}$ and *Adamts10*$^{-/-}$ mice. qRT-PCR analysis showed that *Adamts6* mRNA was not altered with respect to wild type levels in *Adamts6*-deficient mice, but consistently increased in *Adamts10*$^{-/-}$ tissues (Figure 1A). *Adamts10* mRNA showed a significant reduction in *Adamts10*$^{-/-}$ tissues, but was unaltered in *Adamts6*$^{-/-}$ tissues (Figure 1A). Furthermore, ADAMTS6 and ADAMTS10 were co-transfected in HEK293F cells an effort to see if one cleaved the other. Neither ADAMTS10 nor furin optimized ADAMTS10 cleaved ADAMTS6 and ADAMTS6 did not cleave ADAMTS10 (Figure 1 – figure supplement 1). These finding raised two possibilities, i) That *Adamts10*$^{-/-}$ phenotypes could have been buffered by a compensating increase in *Adamts6* mRNA and activity, and ii) That potentially cooperative functions, such as were previously identified in other combined mutants of homologous ADAMTS proteases (Mead et al., 2018b, Nandadasa et al., 2019), may be revealed in *Adamts6*$^{-/-}$;*Adamts10*$^{-/-}$ mice. Therefore, after initial characterization of the *Adamts6* mutant mice, we analyzed the combined null mutants. Each mutant genotype was recovered at the expected Mendelian ratio at the end of the embryonic period (Figure 1 – figure supplement 2).

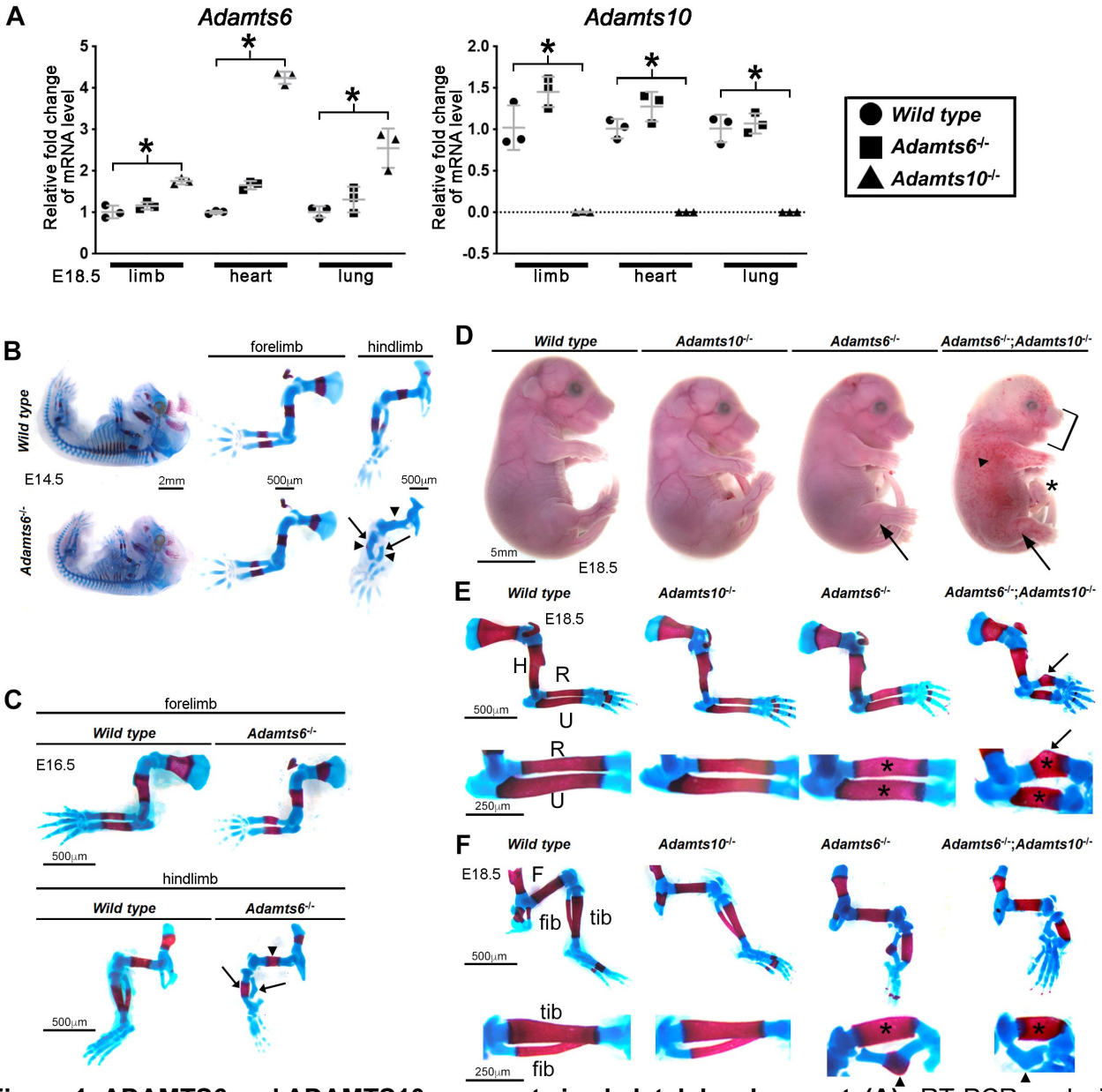

Figure 1: ADAMTS6 and ADAMTS10 cooperate in skeletal development. (A) qRT-PCR analysis of *Adamts6* and *Adamts10* mRNA levels in wild type, *Adamts6*$^{-/-}$ and *Adamts10*$^{-/-}$ limb, heart and lung show that *Adamts6* mRNA is elevated in *Adamts10*$^{-/-}$ tissues, whereas *Adamts10* mRNA is not significantly altered in *Adamts6*$^{-/-}$ tissues (n=3). Error bars represent ± SEM. *P ≤ 0.01, Student's *t* test). **(B, C)** E14.5 **(B)** and E16.5 **(C)** alcian blue- and alizarin red-stained skeletons show severely short and under-ossified *Adamts6*$^{-/-}$ hindlimb skeleton (arrowheads) with severely distorted tibia and fibula (arrow). *Adamts6*$^{-/-}$ forelimbs are not as severely affected as hindlimbs. **(D)** E18.5 *Adamts6*$^{-/-}$;*Adamts10*$^{-/-}$ embryos have severely malformed hindlimbs (arrows), shorter forelimbs, short snout and mandibular hypoplasia (bracket) an omphalocele (asterisks) and widespread cutaneous hemorrhage (arrowhead) compared to *Adamts6*$^{-/-}$ and *Adamts10*$^{-/-}$ embryos. **(E, F)** Alcian blue- and alizarin red-stained *Adamts6*$^{-/-}$;*Adamts10*$^{-/-}$ forelimbs **(E)** and hindlimbs **(F)** show an unremodeled, thickened (asterisks) and shortened long bones (H, humerus; F, femur; U, ulna; R, radius; Tib, tibia; Fib, fibula) with a bent radius (arrow) and tibia (arrowhead). Note the unossified fibula in the *Adamts6*$^{-/-}$;*Adamts10*$^{-/-}$ hindlimb.

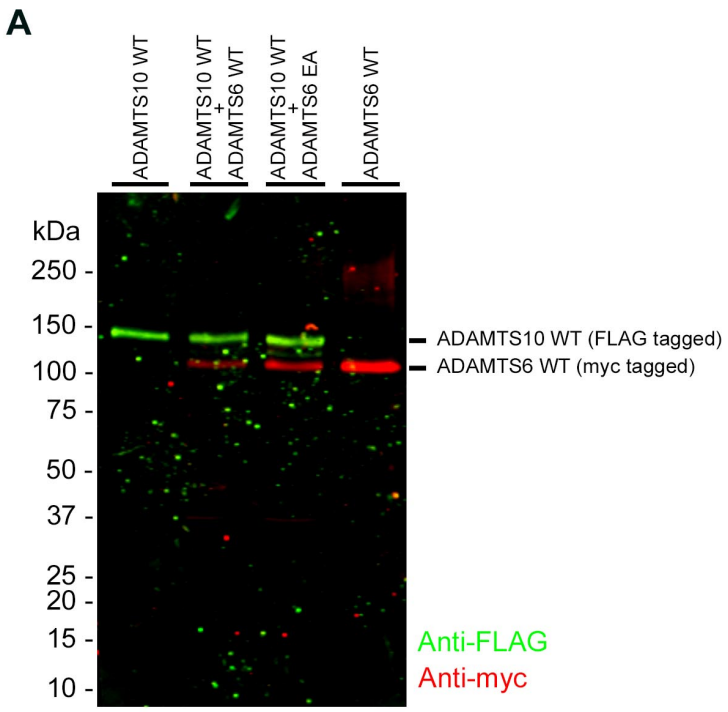

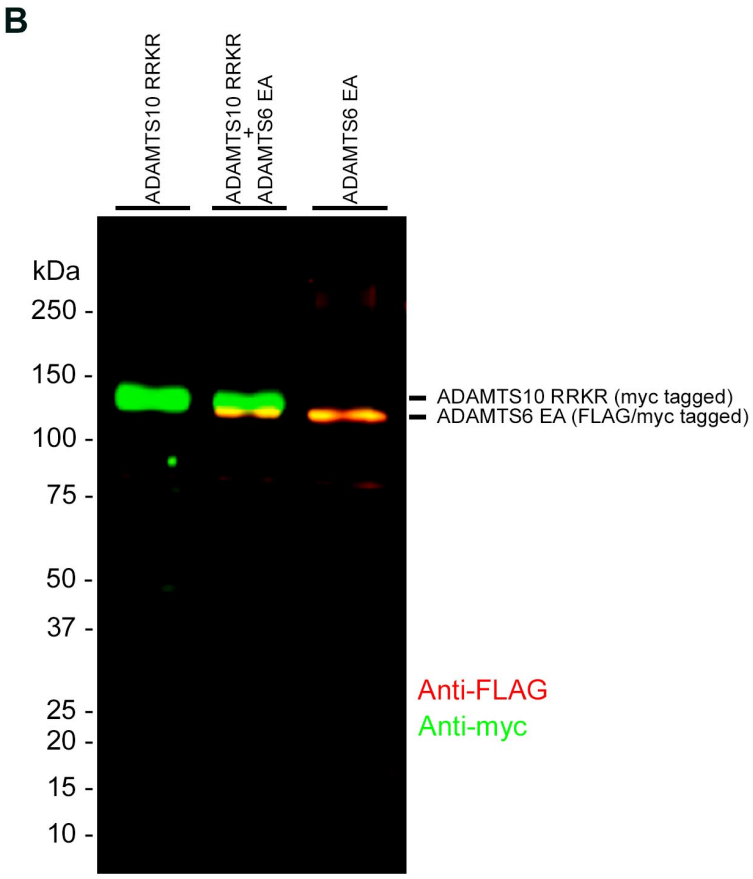

Figure 1 - figure supplement 1. ADAMTS6 and ADAMTS10 do not cleave each other. (A) ADAMTS10 was co-transfected with ADAMTS6 or ADAMTS6 EA mutant. **(B)** Furin-site optimized ADAMTS10 (ADAMTS10-RRKR) was co-transfected with ADAMTS6 EA. No cleavage products of either ADAMTS6 or ADAMTS10 were identified.

Adamts6$^{-/-}$ embryos had severe reduction of crown to rump length, which was also statistically significant in *Adamts10*$^{-/-}$ mice (Figure 1 – figure supplement 3). Whereas *Adamts6*$^{-/-}$ forelimbs appeared shorter, *Adamts6*$^{-/-}$ hindlimbs were not only short, but severely internally rotated (Figure 1B, C, D, F, Figure 1 – figure supplement 3). Alizarin red- and alcian blue-stained skeletal preparations at embryonic day (E)14.5, when ossification is initiated, and at E16.5 and E18.5, when it is well established, showed reduced ossification of *Adamts6*$^{-/-}$ hindlimb distal long bones and deformation of all hindlimb segments, (Figure 1B, C, F), most

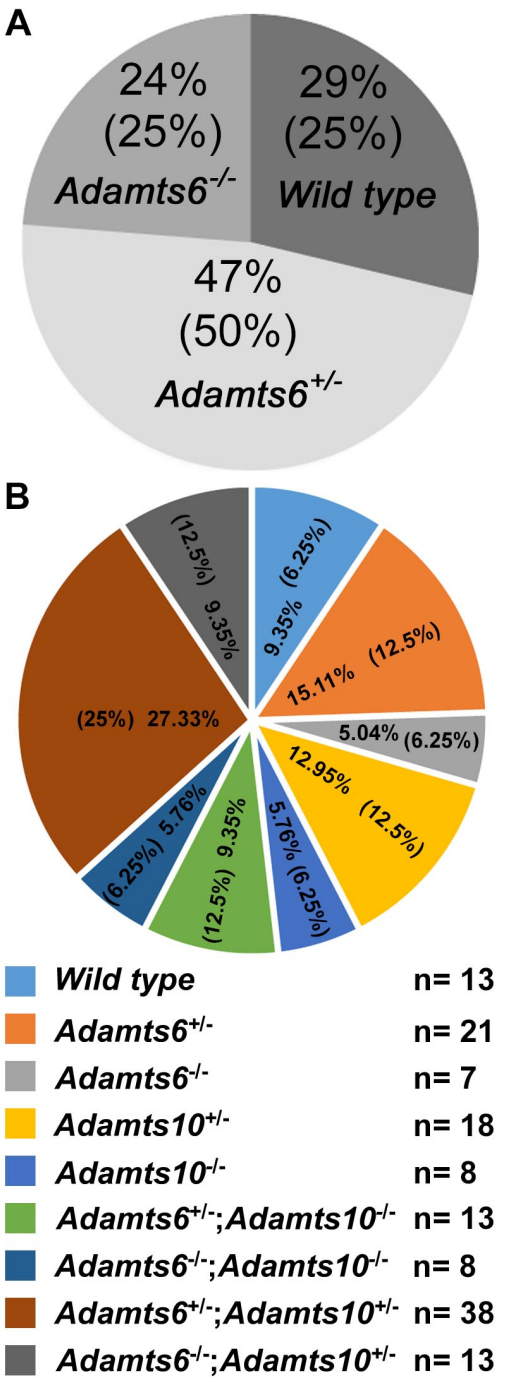

evidently by thicker, angulated tibia and fibula (Figure 1B, C, F, arrows). *Adamts6*$^{-/-}$ embryos demonstrated a failure of diaphyseal modeling in the forelimb (e.g., wider, tubular radius and ulna) and smaller ossific centers, but the skeletal elements were less severely affected than hindlimbs. Neither forelimbs nor hindlimbs showed defects in limb skeletal patterning. In contrast to *Adamts6*$^{-/-}$ embryos, *Adamts10*$^{-/-}$ embryos had mild limb shortening as previously described (Mularczyk et al., 2018b, Wang et al., 2019). The axial and craniofacial skeleton were also abnormal in E18.5 *Adamts6*$^{-/-}$ mice, with shortened tubular ribs, lack of sternal segmentation and an under-ossified xiphoid process (Figure 2). Additionally, their vertebral bodies were smaller in size with a corresponding reduction in the size of all vertebral ossification centers. *Adamts6*$^{-/-}$ craniofacial skeletons had reduced anterior-posterior and nasal-occipital dimensions, corresponding reduction in size of

Figure 1 - figure supplement 2. Predicted Mendelian ratios are observed in mouse crosses. Mendelian ratios obtained from *Adamts6*$^{+/-}$ intercrosses **(A)** and *Adamts6*$^{+/-}$*;Adamts10*$^{+/-}$ intercrosses at E18.5 **(B)** are shown. Observed and expected (in parentheses) genotype percentages are shown in the pie-charts. The actual number of mice used in the analysis is illustrated below the pie-charts.

craniofacial skeletal elements, delayed ossification of parietal and other bones and wider anterior fontanelles (Figure 2).

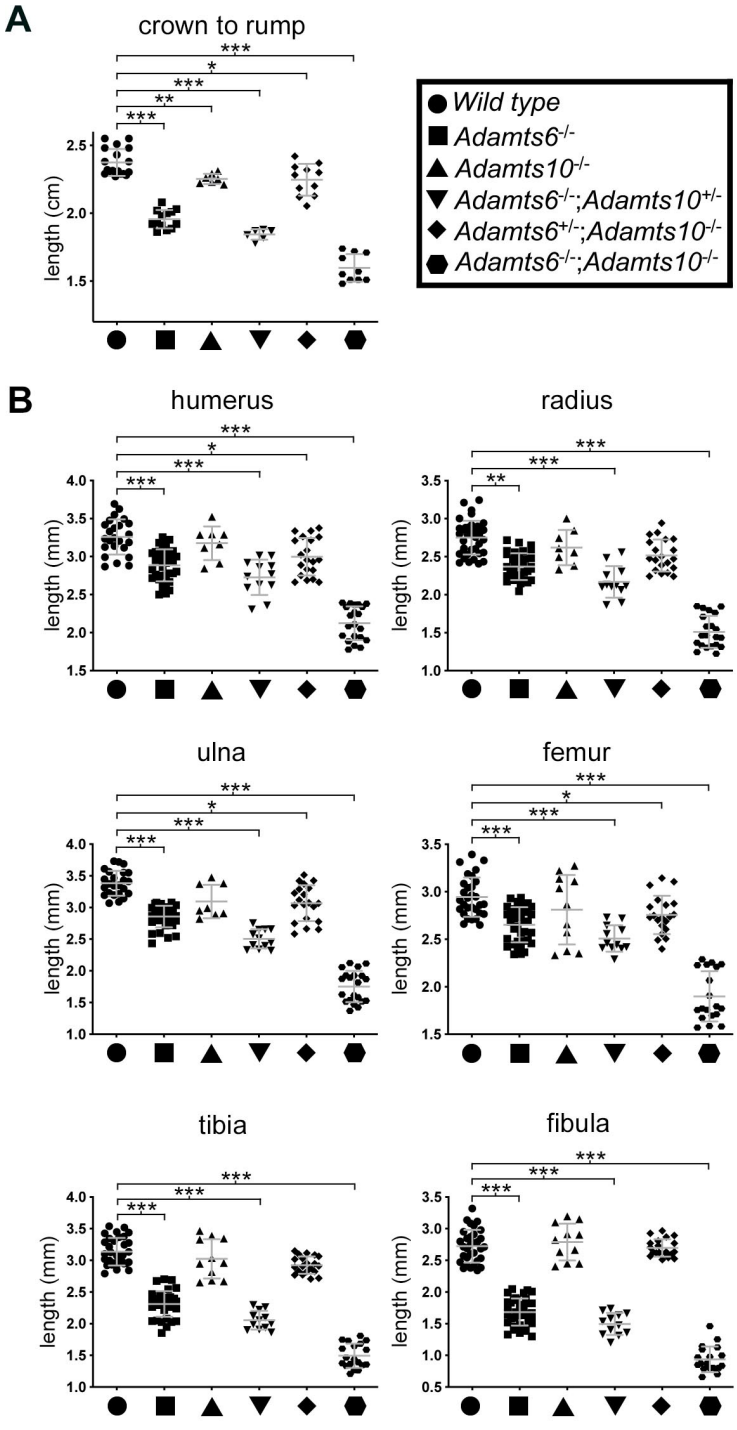

Figure 1 – figure supplement 3. Reduced growth and shorter limb skeletal elements in *Adamts6*- and *Adamts10*-deficient mice. (A) E18.5 *Adamts6*- and *Adamts10*-deficient embryos and embryos with various combinations of alleles have reduced crown-rump length as compared to wild type embryos. **(B)** Embryos with various combinations of the *Adamts6*-mutant allele have shorter long bones than wild type, as shown. *Adamts10*$^{-/-}$ long bones were not significantly shorter than those of wildtype littermates. Crown-rump length, n≥ 6; bone length, n≥ 8. *≤0.05; **≤0.01; ***≤0.001.

Histologic comparison of alcian blue-stained E14.5 wild type and *Adamts6*$^{-/-}$ long bone sections showed delayed endochondral ossification, with persistence of hypertrophic chondrocytes and lack of vascular invasion in the primary ossification centers of long bones such as the femur (Figure 3A). E18.5 alcian blue-stained sections reveal under-ossified and malformed *Adamts6*$^{-/-}$ tibia and fibula (Figure 3B). *Adamts6*-deficient E18.5 distal femoral and proximal tibial cartilage had an expanded hypertrophic chondrocyte zone identified

morphologically and by staining with anti-collagen X, which is specifically expressed in hypertrophic chondrocytes (Figure 3C, D, E).

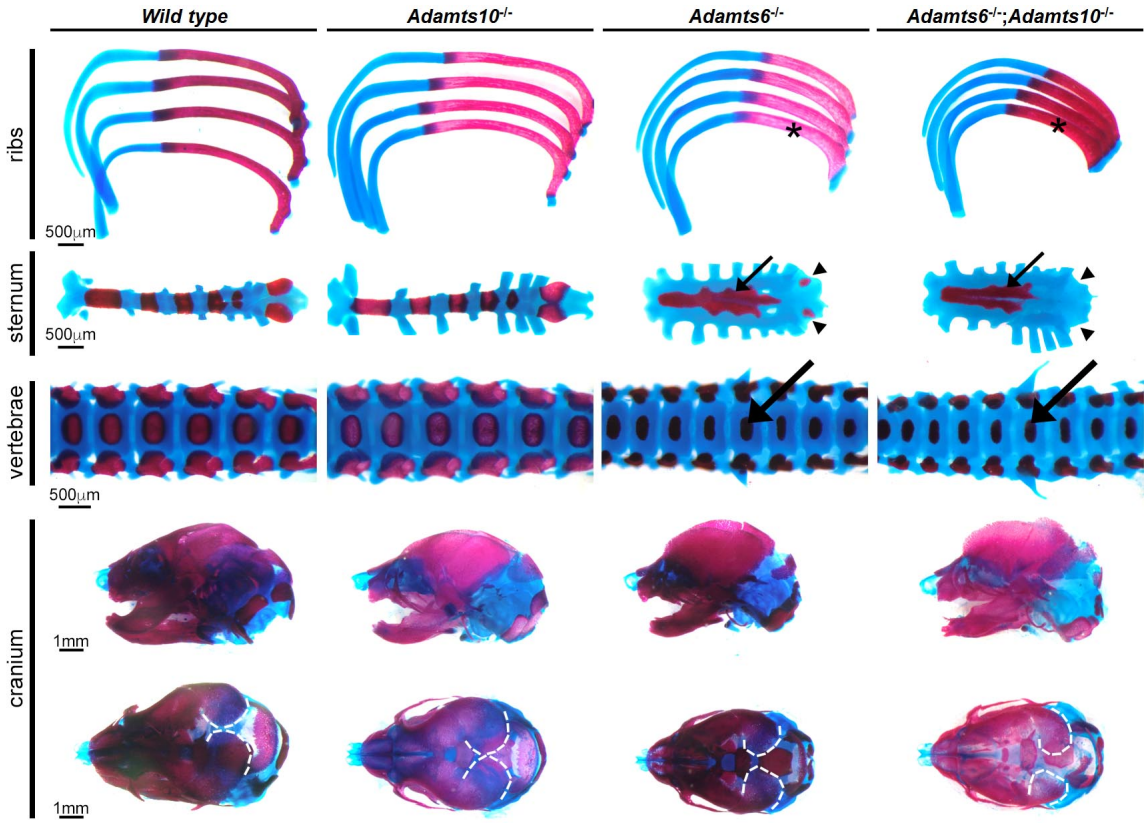

Figure 2: *Adamts6*-deficient embryos have a severely underdeveloped axial skeleton. Alcian blue- and alizarin red-stained E18.5 axial skeleton and craniofacial skeletal preparations show that *Adamts6*$^{-/-}$ and *Adamts6*$^{-/-}$;*Adamts10*$^{-/-}$ embryos have shortened, stout ribs (asterisks), shortened and disorganized manubrium and sternum (small arrows) (note the under-ossified xiphoid process (arrowheads)), smaller vertebral bodies (large arrows), and a smaller cranium with delayed mineralization of parietal bones (dashed white lines).

To determine cooperative roles of ADAMTS6 and ADAMTS10, we obtained mice with combinations of the two mutant alleles. *Adamts6*$^{-/-}$;*Adamts10*$^{-/-}$ embryos demonstrated markedly more severe anomalies than *Adamts6*$^{-/-}$ mutants including subcutaneous hemorrhage, micrognathia and an omphalocele, along with severe forelimb and hindlimb dysmorphology (Figure 1D). Skeletal preparations and alcian blue-stained sections showed more severe hindlimb anomalies than in *Adamts6*$^{-/-}$ mutants and appearance of forelimb abnormalities similar in severity to those of the hindlimbs of *Adamts6*$^{-/-}$ mutants, with externally evident shortening, and the

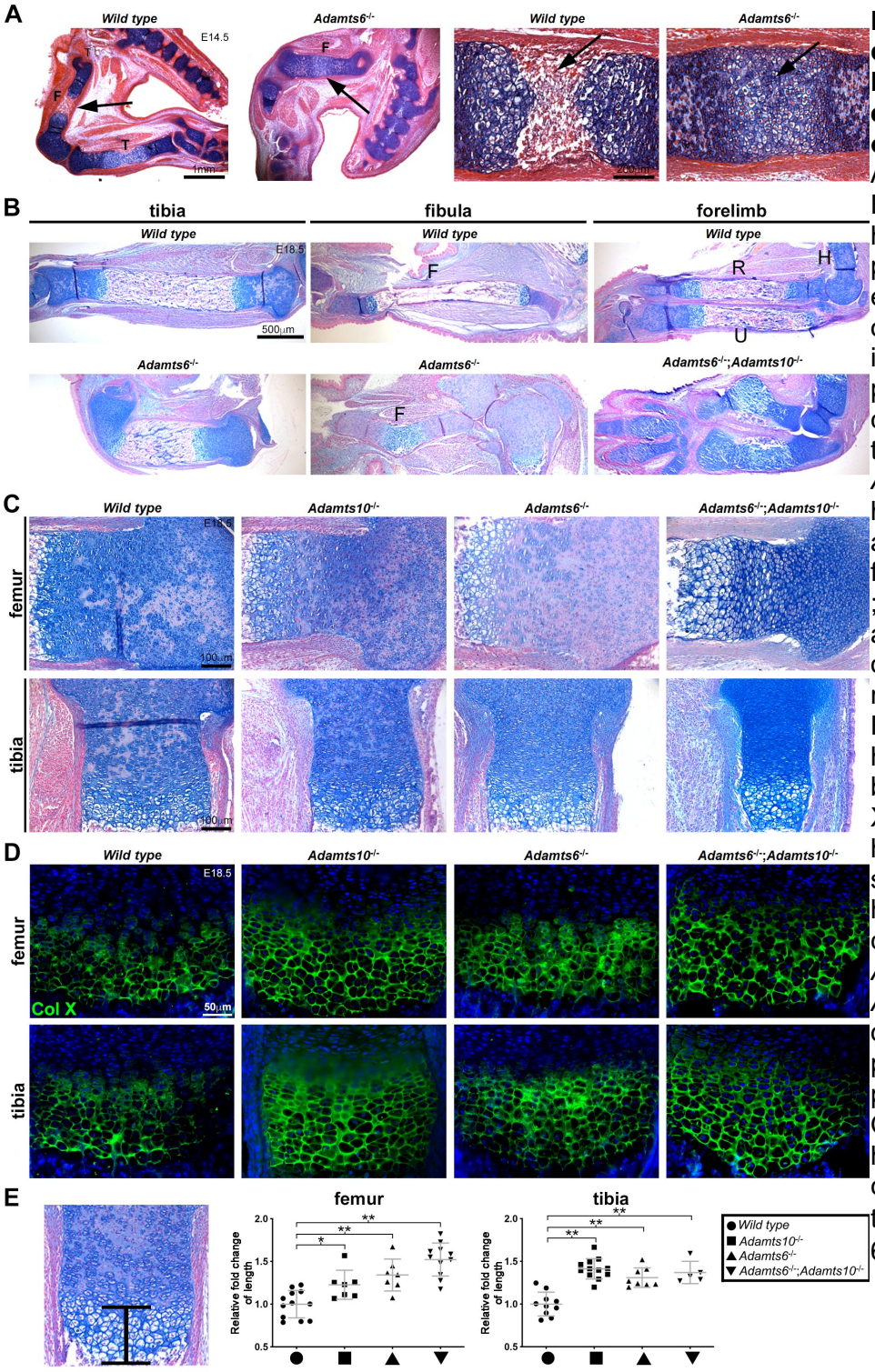

Figure 3: Adamts6-deficent hindlimbs have delayed endochondral ossification. (A) Alcian blue-stained E14.5 *Adamts6*$^{-/-}$ hindlimbs have primitive skeletal limb elements with a non-ossified femur (arrows indicate the femoral primary ossification center). F, femur; T, tibia. **(B)** E18.5 *Adamts6*$^{-/-}$ hindlimbs have malformed tibia and under-ossified fibula. *Adamts6*$^{-/-}$;*Adamts10*$^{-/-}$ radius and tibia are under-ossified and malformed. F, fibula; R, radius; U, ulna; H, humerus. **(C-D)** Alcian blue **(C)** and Collagen X **(D)** stained E18.5 hindlimb sections show an extended hypertrophic chondrocyte zone in *Adamts6*$^{-/-}$ and *Adamts6*$^{-/-}$;*Adamts10*$^{-/-}$ distal femoral and proximal tibial growth plates. **(E)** Quantification of hypertrophic chondrocyte zone in the femur and tibia. n≥ 6. *≤0.05; **≤0.01.

greatest reduction of nose-rump length and the shortest long bones among all the generated genotypes (Figure 1D-F, Figure 3B, Figure 1 – figure supplement 2). Fibular ossification was minimal, and the zeugopod was angulated with pronounced tibial torsion (Figure 1F). The shortened and tubular ribs, vertebral bodies with

smaller ossification centers, total lack of xiphoid process ossification and poor ossification of cranial bones resulting in larger fontanelles, further demonstrated greater severity of skeletal malformations than observed in *Adamts6*$^{-/-}$ embryos (Figure 2). Whereas inactivation of one *Adamts6* allele in *Adamts10*$^{-/-}$ mice did not significantly worsen the observed dysmorphology and skeletal phenotype, *Adamts10* haploinsufficiency further shortened *Adamts6*$^{-/-}$ humerus, radius, ulna and femur (Figure 1 – figure supplement 2). Taken together, these observations suggest a cooperative role of ADAMTS6 and ADAMTS10 in skeletal development, with ADAMTS6 making the greater contribution of the two proteases.

Adamts6 and Adamts10 have overlapping expression in skeletal tissue

To follow up on prior publications showing strong expression of *Adamts6* in the heart and of *Adamts10* in multiple embryo and adult tissues (PrinsMead et al., 2018, Somerville, Jungers et al., 2004, Wang et al., 2019) as well as immunohistochemical localization of ADAMTS10 in limb growth cartilage, perichondrium and muscle (Mularczyk, Singh et al., 2018a), we compared the spatial and temporal localization of their mRNAs at different stages of limb development using RNAScope in situ hybridization (*Adamts6*) and an intragenic lacZ reporter (*Adamts10*). *Adamts6* and *Adamts10* exhibited overlapping expression in resting and proliferating zone chondrocytes and perichondrium of E13.5 and E14.5 hindlimb long bones (Figure 4). At E14.5, both genes were expressed at sites of vascular invasion in the primary centers of ossification (Figure 4B, arrowheads). *Adamts6* expression was also noted in tendons and skeletal muscle around the knee joints and *Adamts10* was ubiquitously expressed throughout the joint interzone (Figure 4A, B).

Fibrillin-2 accumulates in Adamts6$^{-/-}$, Adamts10$^{-/-}$ and Adamts6$^{-/-}$;Adamts10$^{-/-}$ hindlimbs

The distribution and staining intensity of fibrillin-2 in *Adamts6*-deficient hindlimbs was assessed by immunostaining with a monospecific fibrillin-2 antibody. As compared to normal fibrillin-2 staining surrounding the femoral head, perichondrium and surrounding soft tissue, *Adamts10*$^{-/-}$

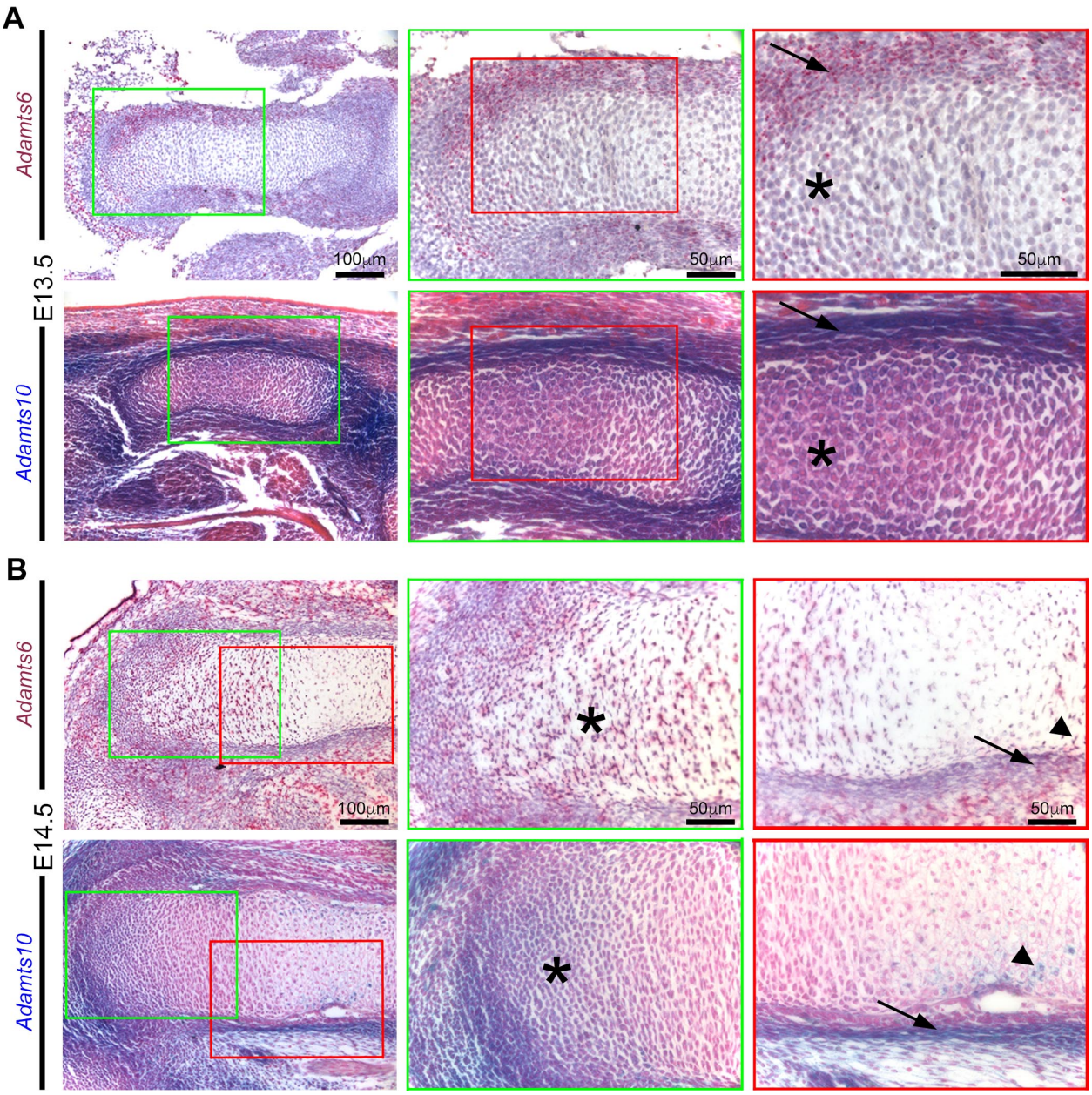

Figure 4: *Adamts6* and *Adamts10* mRNAs show overlapping expression in the developing hindimbs. *Adamts6* (RNA in situ hybridization (red signal)) and *Adamts10* (β-gal staining of *Adamts10*$^{+/-}$ tissues, blue nuclei) show expression in the E13.5 **(A)** and E14.5 **(B)** perichondrium (arrows), resting chondrocytes (asterisks) and peripheral hypertrophic chondrocytes at the site of vascular invasion (arrowheads).

and *Adamts6*$^{-/-}$ hindlimbs have increased staining intensity and overall expanded fibrillin-2 distribution (Figure 5A). *Adamts6*$^{-/-}$;*Adamts10*$^{-/-}$ hindlimbs showed an even greater fibrillin-2 staining intensity, suggesting that fibrillin-2 accumulated in the absence of ADAMTS6 and ADAMTS10 (Figure 5A). There was no consistent change in fibrillin-1 staining in either *Adamts6*-

or *Adamts10*-deficient hindlimbs (Figure 5 – figure supplement 1A). *Fbn1* and *Fbn2* mRNA levels were unchanged in *Adamts6*- and *Adamts10*-deficient hindlimbs, suggesting that increased fibrillin-2 staining was not a result of increased transcription (Figure 5B, Figure 5 – figure supplement 1B).

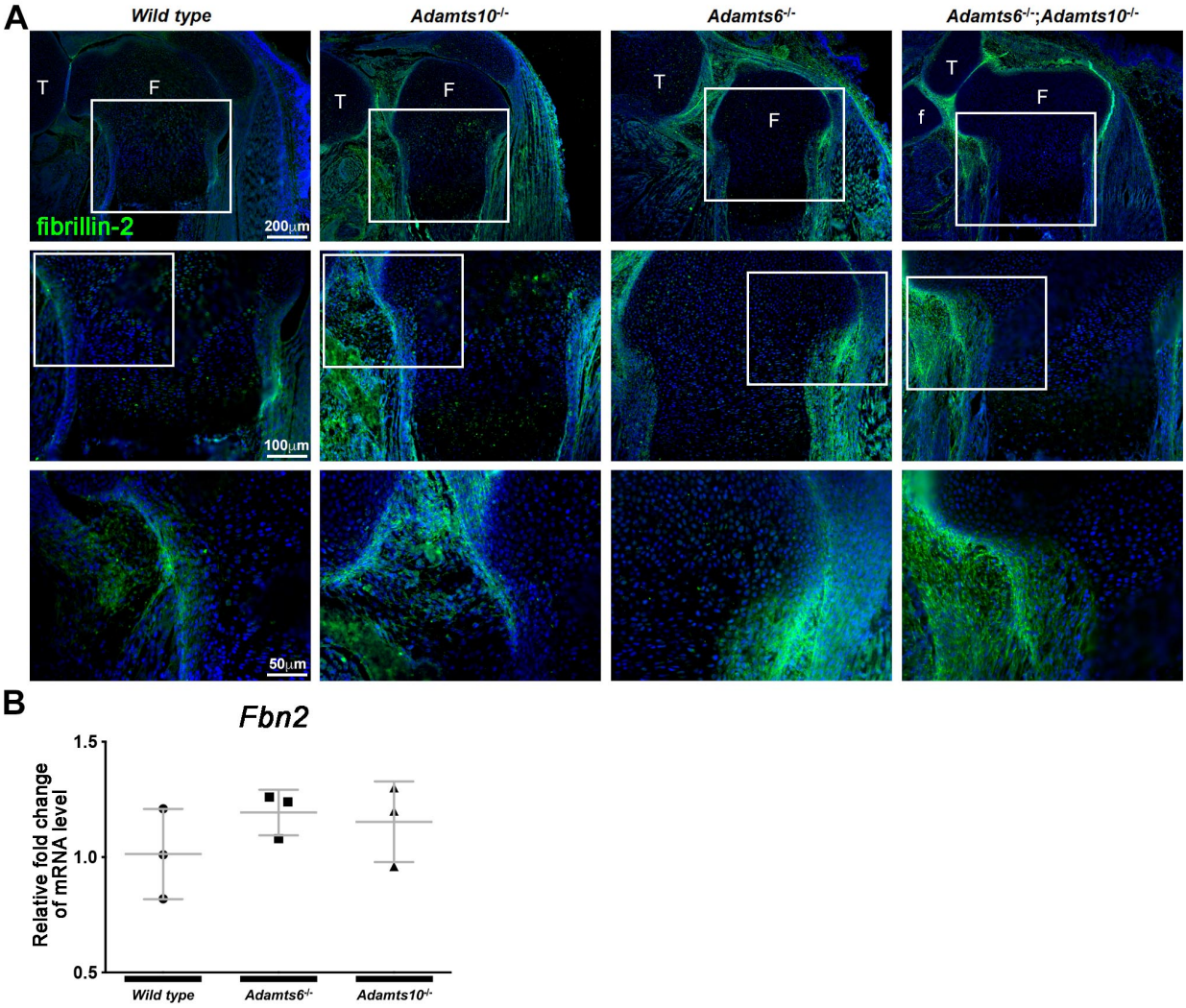

Figure 5: Increased fibrillin-2 staining in *Adamts6*-deficient limbs. (A) Increased staining intensity (green) of fibrillin-2 in E18.5 *Adamts6*- and *Adamts10*-deficient hindlimbs. Sections are counterstained with DAPI (blue). F, femur; T, tibia; f, fibula. **(B)** No change in *Fbn2* RNA levels in *Adamts6*$^{-/-}$ or *Adamts10*$^{-/-}$ E18.5 hindlimbs. n=3.

Adamts6 binds to fibrillin-2 microfibrils

Co-expression and functional cooperation between ADAMTS6 and ADAMTS10, taken together with the strong genetic and biochemical association of ADAMTS10 with fibrillin-2 turnover

(Mularczyk et al., 2018a, Wang et al., 2019), led us to investigate ADAMTS6 binding to microfibrils in *Fbn1*$^{-/-}$ mouse embryo fibroblasts (MEFs), which assemble microfibrils comprising fibrillin-2, but not fibrillin-1. Co-cultures of *Fbn1*$^{-/-}$ MEFs with HEK293T cells stably expressing catalytically inactive ADAMTS6 (ADAMTS6Glu^{404}Ala, referred to as ADAMTS6 EA) for 6 days illustrated specific co-localization of ADAMTS6 EA with fibrillin-2 microfibrils (Figure 6A). When *Fbn1*$^{-/-}$ MEFs were co-cultured with HEK293F cells expressing active ADAMTS6, no fibrillin-2 staining was obtained, suggestive of proteolytic destruction of fibrillin-2 microfibrils (Figure 6A). *Adamts6*$^{-/-}$ MEFs showed greater fibrillin-2 microfibril abundance and staining intensity than wild type MEFs (Figure 6B). Together, these findings suggest that ADAMTS6 co-localizes with and could bind to and proteolytically cleave fibrillin-2 microfibrils.

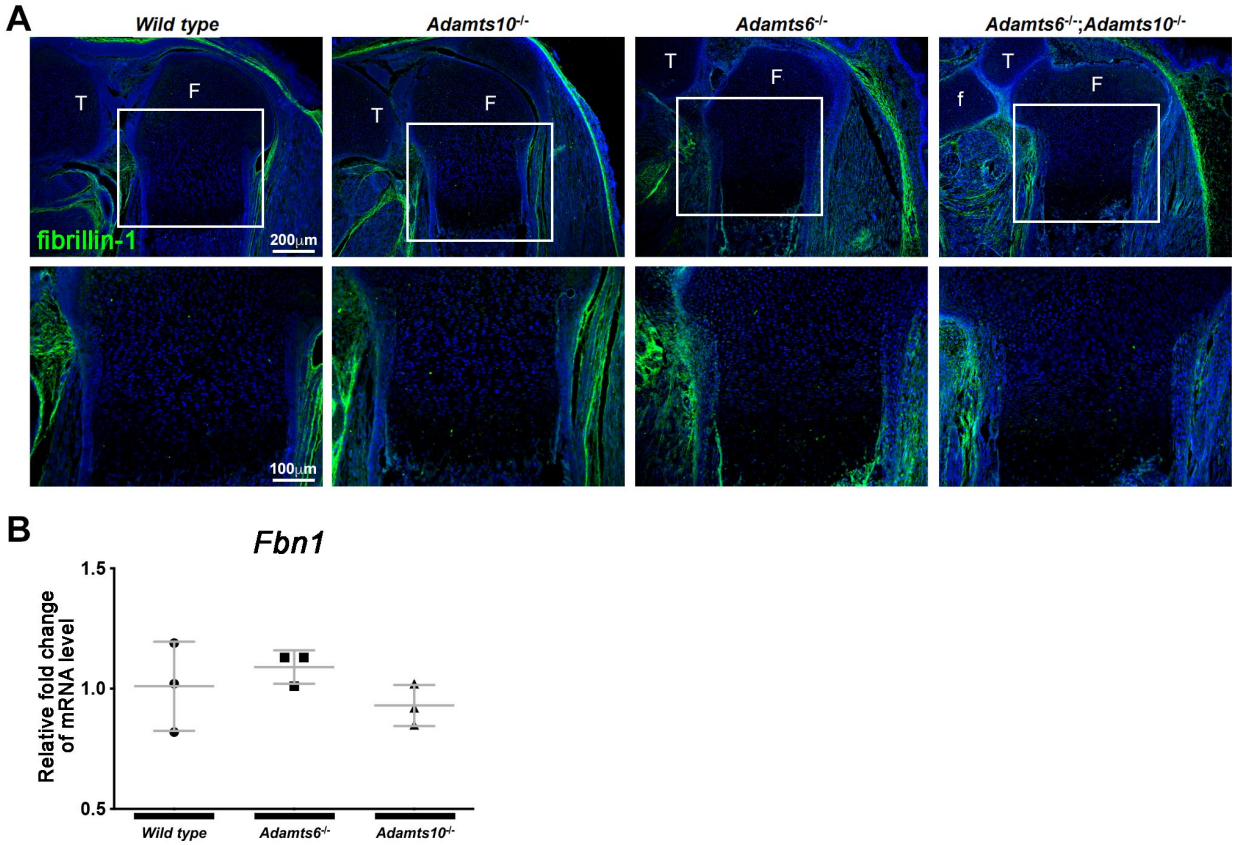

Figure 5 – figure supplement 1: No change in fibrillin-1 staining in *Adamts6*-deficient limbs. **(A)** Similar staining intensity (green) of fibrillin-1 was seen in E18.5 *Adamts6*- and *Adamts10*-deficient hindlimbs. Sections are counterstained with DAPI (blue). F, femur; T, tibia; f, fibula. **(B)** No change in *Fbn1* RNA levels in *Adamts6*$^{-/-}$ or *Adamts10*$^{-/-}$ E18.5 hindlimbs. n=3.

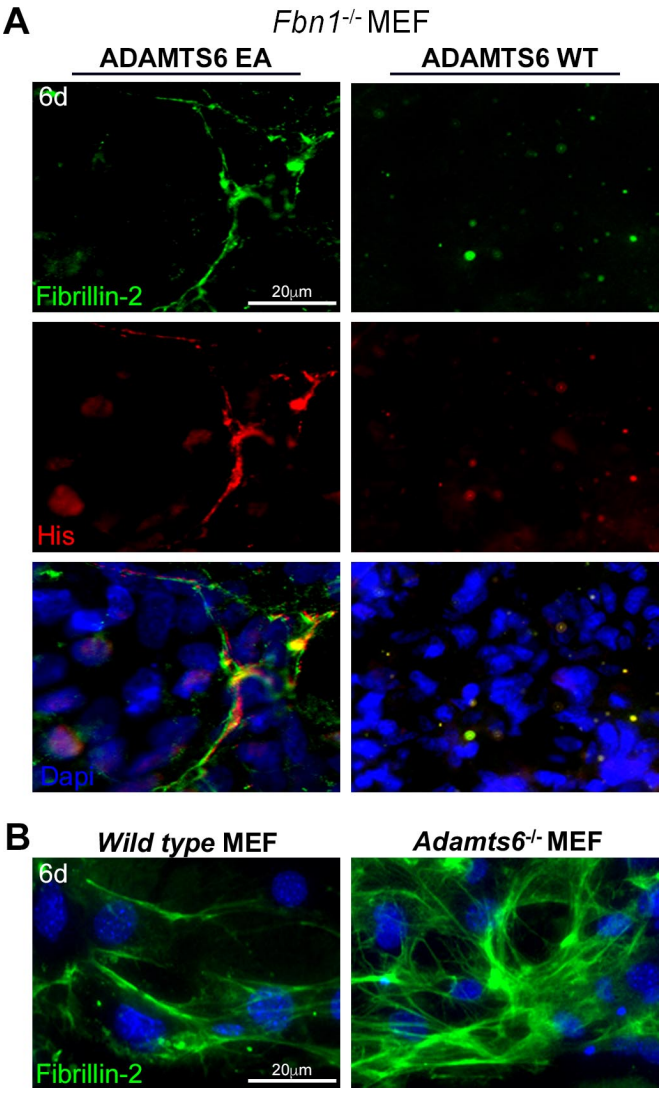

Figure 6: Loss of fibrillin-2 microfibrils in the presence of ADAMTS6. (A) *Fbn1*-deficient mouse embryonic fibroblasts (MEFs), which only express fibrillin-2, were co-cultured with human embryonic kidney (HEK293) cells overexpressing 6XHis-tagged wild type ADAMTS6 (ADAMTS6 WT) or the catalytically inactive mutant, ADAMTS6 EA. Fibrillin-2 (green) co-localized with anti 6XHis (His)-tagged ADAMTS6 EA (red), but no microfibrils were observed in the presence of wild type ADAMTS6 (red). **(B)** Increased fibrillin-2 (green) microfibril staining and greater staining intensity were obtained in *Adamts6*$^{-/-}$ MEFs than in wild type MEFs. The cell nuclei are stained with DAPI (blue) in all images.

Since fibrillin microfibrils contain additional components beside fibrillins (Cain, Morgan et al., 2006, De Maria, Wilmarth et al., 2017, Fujikawa, Yoshida et al., 2017, Mecham & Gibson, 2015), which could be responsible for their binding to ADAMTS6, we asked whether purified ADAMTS6 constructs bound directly to purified fibrillin-2 in binary interaction assays. Biacore analysis showed that C-terminal ADAMTS6 constructs (ADAMTS6-Ct, ADAMT6-S4TSR and ADAMTS6-4TSR) bound the C-terminal half of fibrillin-2 (fibrillin-2-Ct) (Figure 7A-C, Table 1). Since all 4TSR-array-containing fragments bound to fibrillin-2-Ct, but ADAMTS6-TCS did not (data not shown), we conclude that the binding region is located in the C-terminal ADAMTS6 TSR array. In reciprocal Biacore analysis using ADAMTS6-Ct as the immobilized ligand, binding to the N- and C-terminal halves of fibrillin-2 was observed (Figure 7D, Table 2). Relatively similar Kd values of 43nM for fibrillin-2-Nt and 80 nM for fibrillin-2-Ct suggested that the ADAMTS6 binding site on fibrillin-2 may lie in the overlapping region of the two fragments between cbEGF22 and cbEGF24. Alternatively,

there could be two binding sites, one in each half with similar affinities for ADAMTS6. Thus, direct ADAMTS6 binding to fibrillin-2, likely explains its co-localization with fibrillin-2 microfibrils.

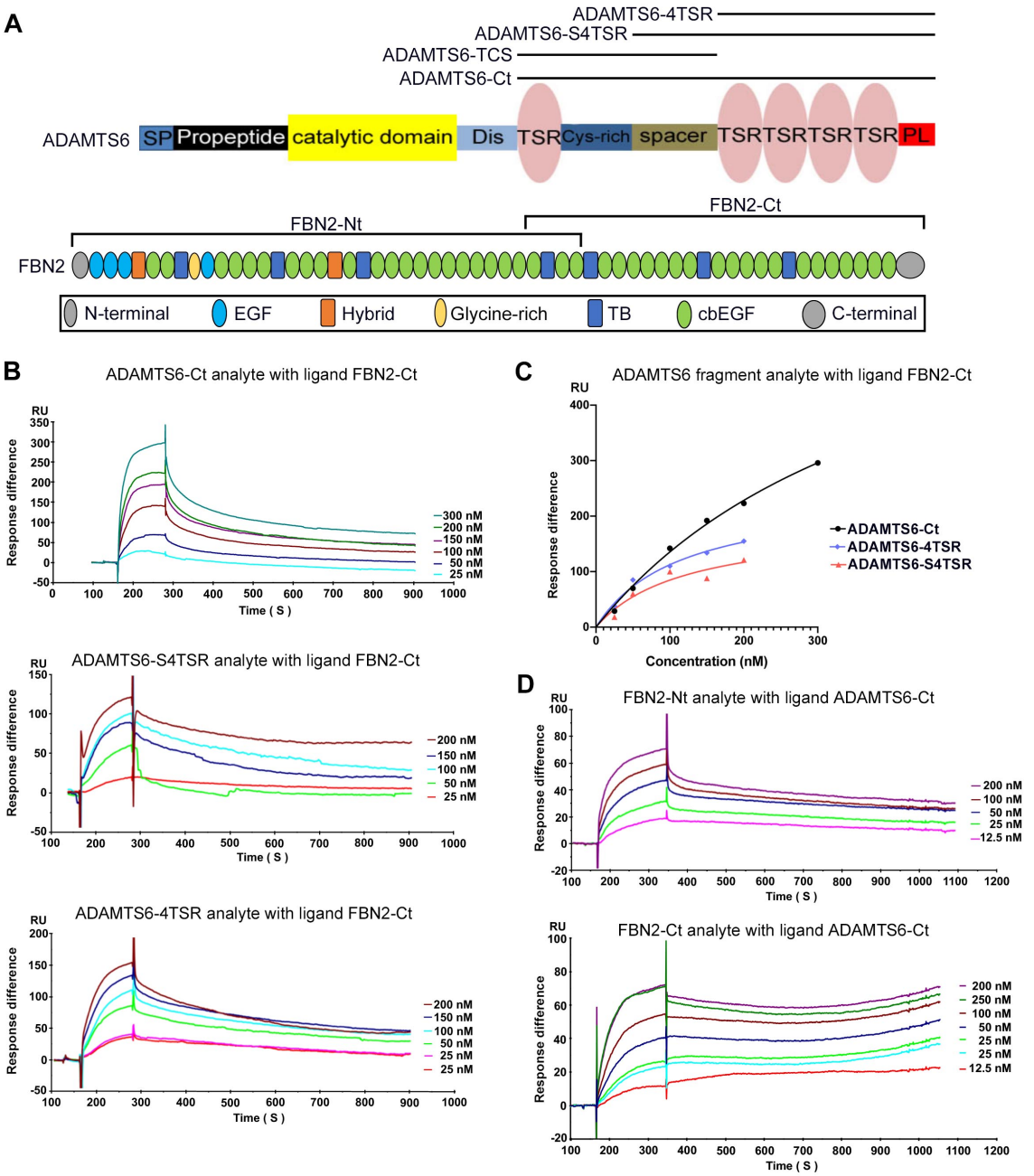

Figure 7: ADAMTS6 binds directly to fibrillin-2. (A) Domain structures of ADAMTS6 and fibrillin-2 are illustrated and indicate the recombinant constructs used in the present work. **(B-C**) Biacore analysis shows dose-dependent binding curves for the ADAMTS6-C-terminal constructs ADAMTS6-Ct, ADAMTS6-4TSR and ADAMTS6-S4TSR against immobilized FBN2-Ct **(B)**, and comparative binding characteristics of the constructs **(C)**. **(D)** A reciprocal Biacore analysis using immobilized ADAMTS6-Ct shows that fibrillin-2-Nt and fibrillin-2-Ct used as the analyte each bind strongly to ADAMTS6-Ct.

Adamts6 cleaves fibrillin-2

ADAMTS10 rendered furin-activatable by optimization of its furin processing site was previously shown to cleave fibrillin-2 and *Adamts10*$^{-/-}$ mice showed accumulation of fibrillin-2 microfibrils in the eye and skeletal muscle (Mularczyk et al., 2018b, Wang et al., 2019). Direct binding of ADAMTS6 constructs to fibrillin-2 protein, ADAMTS6 EA co-localization with fibrillin-2 microfibrils, loss of fibrillin-2 microfibrils in vitro in the presence of wild type ADAMTS6, and increased fibrillin-2 staining in *Adamts6*-deficient hindlimbs suggests that fibrillin-2 is also an ADAMTS6 substrate. HEK293F cells stably expressing the N- or C-terminal halves of fibrillin-2 were transfected with either ADAMTS6 WT or ADAMTS6 EA and the serum-free conditioned medium was collected for Terminal Amine Isotopic Labeling of Substrates (TAILS), an N-terminomics approach for identifying protease substrates and cleavage sites (Kleifeld, Doucet et al., 2010, Kockmann, 2016), which has recently been applied for identification of ADAMTS substrates (Bekhouche, Leduc et al., 2016) (Figure 8A). Proteins were labeled with stable isotopes of formaldehyde (natural (CH_2O)/light isotope applied to the ADAMTS6-containing medium or isotopically heavy ($^{13}CD_2O$), applied to the ADAMTS6 EA-containing medium). The ensuing reductive dimethylation labels and blocks free protein N-termini as well as lysine sidechains. Labeled proteins from each such pair of digests were combined, further digested with trypsin and filtered through a hyperbranched polyglycerol aldehyde polymer which binds to free N-termini generated by trypsin (Figure 8A), reserving the peptides with blocked and labeled N-termini for mass spectrometry. Following mass spectrometry, a targeted search for fibrillin-2 peptides with labeled N-termini revealed a putative cleavage site in the fibrillin-2 C-terminal half at the Gly^{2158}-His^{2159} peptide bond in a linker between TGFβ binding-like domain 6 and epidermal growth factor (EGF) repeat 32 (Figure 8B-F). The peptide sequence and presence of an N-terminal label was confirmed with high confidence by the MS^2 spectrum (Figure 8C). Quantification of peptide ion abundance in the sample containing

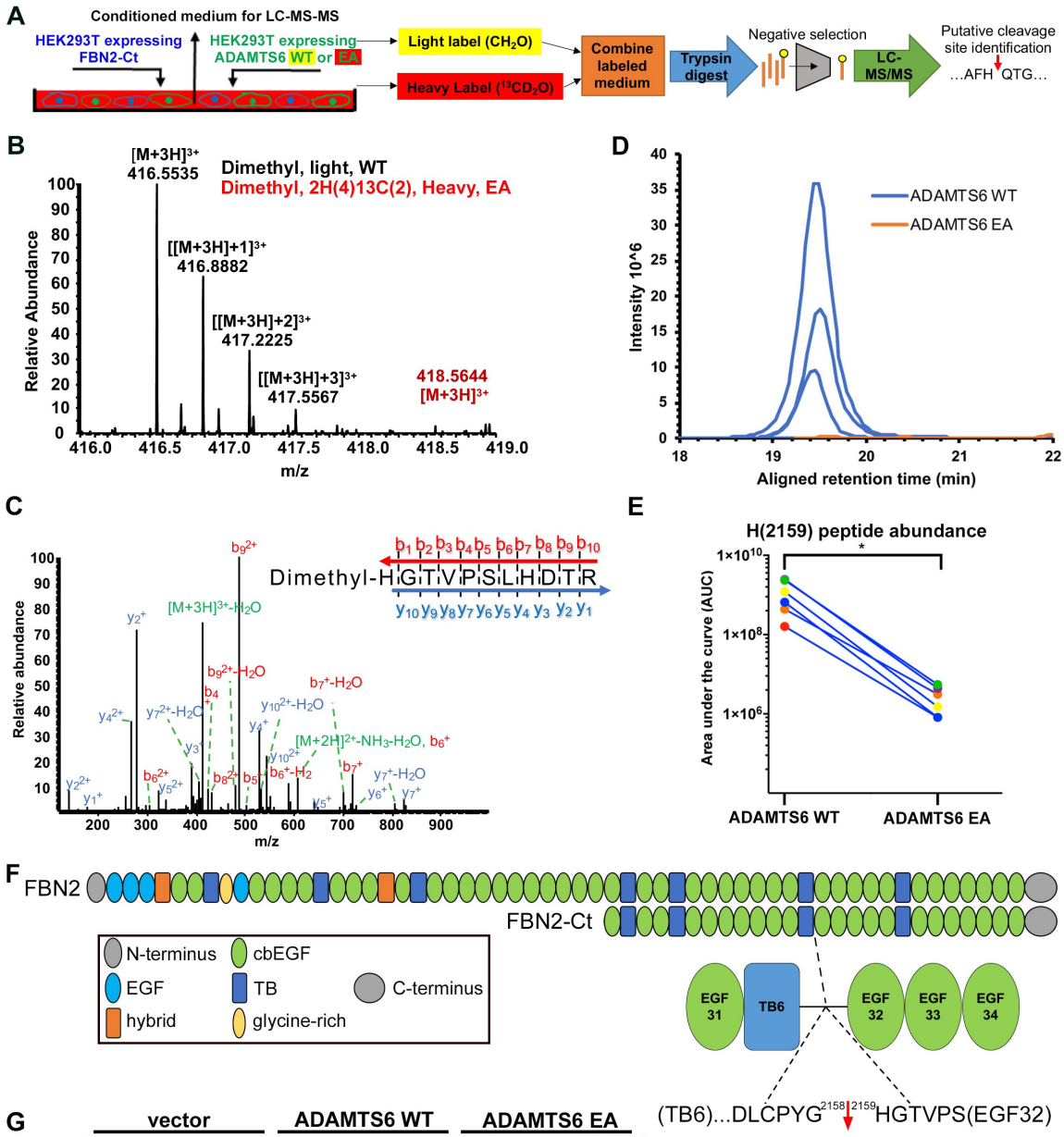

Figure 8: Fibrillin-2 cleavage by ADAMTS6 and identification of the cleavage site using N-terminomics. (A) Schematic of the experimental approach. Proteins from conditioned medium after co-culture of HEK293F cells stably expressing FBN2-Ct and cells expressing either ADAMTS6 WT or ADAMTS6 EA (inactive) were labeled by reductive dimethylation using stable formaldehyde isotopes and analyzed by LC-MS/MS in the TAILS workflow described in detail in the Methods section. **(B)** MS spectrum of the parent ions used for ADAMTS6 WT (black) or ADAMTS6 EA (red) quantitation. (**C**) Annotated MS/MS ion spectrum of the light dimethyl peptide, showing b- (N-terminus preserved) and y-type (C-terminus preserved) ions generated by amide bond cleavage during collisional-induced dissociation that were used to derive the peptide sequence indicated at the top right. **(D)** Retention time-aligned extracted ion chromatographs (EICs) comparing abundance of the light dimethyl-labeled HGTVPSLHDTR peptide (blue) in ADAMTS6 WT medium and isotopically heavy dimethyl-labeled peptide (orange) in ADAMTS6 EA medium from the 3 TAILS replicate experiments. **(E)** The area under the EICs was quantified and comparison of ion abundance is shown in a dumbbell plot (from the 3 TAILS and the 3 pre-TAILS replicates). Significance was determined using a two-tailed, paired Student t-test, * indicates *P*-value < .05. **(F)** Domain structure of fibrillin-2 and the C-terminal construct FBN2-Ct showing the location of the cleaved peptide bond Gly^{2158}-His^{2159} in the linker between TB6 and EGF32. **(G)** Orthogonal validation of fibrillin-2 cleavage by ADAMTS6 using western blot analysis of the conditioned medium from A, shows distinct molecular species (100 kDa and 75 kDa) reactive with anti-fibrillin-2-Ct antibody (green, N-terminal fragment of fibrillin-2-Ct) and C-terminal anti-His_6 antibody (red, C-terminal fragment of fibrillin-2-Ct), respectively, obtained in the presence of ADAMTS6 WT, but not ADAMTS6 EA, indicative of fibrillin-2-Ct cleavage. The green band of ~350 kDa is endogenous fibrillin-2 produced by HEK293T cells. The yellow band at ~175 kDa indicates overlapping anti-His_6 and anti-fibrillin-2 Ct antibody staining of full-length fibrillin-2-Ct. Cells transfected with empty vector were used to obtain control medium.

ADAMTS6 versus ADAMTS6 EA showed a considerable excess of this peptide in the presence of active ADAMTS6 (Figure 8D-E). Western blot of the medium from these experiments showed that ADAMTS6 cleaved the C-terminal half of fibrillin-2 (Figure 8G), but not the N-terminal half (data not shown). The cleavage products of 100 kDa and 75 kDa matched the predicted cleavage fragments and added up to the expected mass of the FBN2-Ct construct (175 kDa). These findings strongly suggested that fibrillin-2 is an ADAMTS6 substrate which could be relevant to the profound skeletal defects observed in *Adamts6*$^{-/-}$ mice. Importantly, the detected cleavage site is located between two domains, resulting in complete separation of the fragments as opposed to cleavage sites within FBN2 domains that might remain linked by disulfide bonds, leading to “nicks’ rather than fragmentation. The cleavage site is consistent with prevention of FBN2 assembly which requires multimerization of the C-terminus downstream of the cleavage site (Hubmacher, El-Hallous et al., 2008).

Fbn2 haploinsufficiency reverses Adamts6 null skeletal defects

To determine whether fibrillin-2 accumulation had a significant role in the observed growth, limb and skeletal anomalies, fibrillin-2 levels were reduced in *Adamts6*-deficient mice by deletion of one *Fbn2* allele. *Fbn2* haploinsufficiency in *Adamts6*-deficient embryos (*Adamts6*$^{-/-}$;*Fbn2*$^{+/-}$) dramatically restored the external hindlimb morphology of *Adamts6* mutants as well as the maturity and length and shape of skeletal components of the hindlimb and axial skeleton (Figure 9). Specifically, alizarin red and alcian blue-stained skeletal preparations demonstrated an appropriately segmented sternum, normal xiphoid process, partial restoration of bone length and improved ossification of hindlimb long bones (Figure 9A, B, Figure 9 – figure supplement 1). In addition, cleft secondary palate which occurred with a high incidence in *Adamts6*$^{-/-}$ embryos did not occur in *Adamts6*$^{-/-}$;*Fbn2*$^{+/-}$ embryos (Figure 9C). Additionally, the growth plate histology appeared comparable to wild type and fibrillin-2 staining in the hindlimb showed reduced intensity comparable to wild type (Figure 9D-F). Therefore, *Fbn2* haploinsufficiency significantly ameliorates limb and skeletal defects in *Adamts6*-deficient embryos. Consistent with the previously defined role of fibrillin-2 in BMP signaling, *Adamts6*$^{-/-}$ hindlimbs had reduced pSmad5 compared to wild type, which was restored to wild type levels in *Adamts6*$^{-/-}$;*Fbn2*$^{+/-}$ hindlimbs (Figure 9 – figure supplement 2). In contrast, *Adamts6*-deficient mice with a 80% reduction in *Fbn1* (in *Adamts6*$^{-/-}$;*Fbn1*$^{mgR/mgR}$ embryos) (Figure 9 – figure supplement 3) had no amelioration of limb defects, suggesting a selective role for ADAMTS6 in regulating fibrillin-2 abundance in limb microfibril proteostasis.

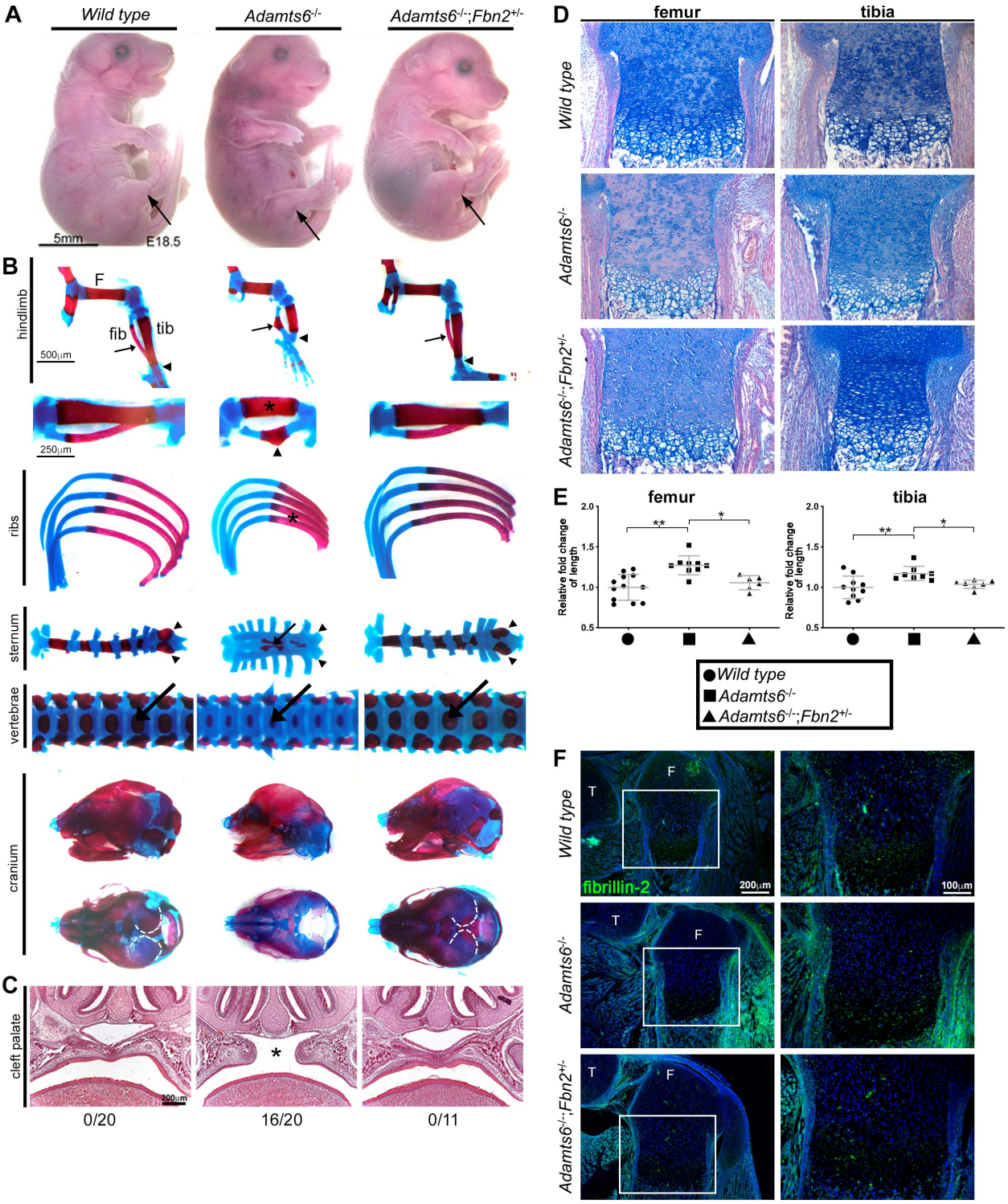

Figure 9: Genetic reversal of limb and craniofacial anomalies of *Adamts6* mutant mice by *Fbn2* haploinsufficiency. (A,B) Deletion of one *Fbn2* allele reverses several anomalies in the *Adamts6*$^{-/-}$ mutants as shown in E18.5 embryos, specifically, restoration of externally evident limb dimensions and reversal of rotational anomaly (arrow) (**A**) and (**B**), overall hindlimb skeletal structure, reversal of internal rotation (arrow) and bone length, restoration of normal tibial and fibular length and alignment as well as larger primary ossification centers in the tibia (tib), fibula (fib), metacarpals and phalanges in *Adamts6*$^{-/-}$;*Fbn2*$^{+/-}$ limbs (two center panels, thin arrows) and restoration of sternal segmental ossific centers (thick arrows) and restoration of length, ossification and relative proportions of the ribs, sternal segments and xiphoid process (arrowheads). **(C)** Hematoxylin and eosin-stained coronal cranial sections from E18.5 embryos show that *Fbn2* haploinsufficiency reverses cleft secondary palate observed in the majority of *Adamts6*$^{-/-}$ mutants (asterisk; incidence listed below the respective panels). **(D)** stained E18.5 hindlimb sections show improved growth plate structure approximating the wild type, and restoration of the hypertrophic chondrocyte zone in *Adamts6*$^{-/-}$;*Fbn2*$^{+/-}$ distal femoral and proximal tibial growth plates. **(E)** Quantification of hypertrophic chondrocyte zone length in the femur and tibia. n≥ 6. *≤0.05; **≤0.01. **(F)** Restoration of fibrillin-2 staining intensity (green) in E18.5 *Adamts6*$^{-/-}$;*Fbn2*$^{+/-}$ hindlimbs. Sections were counterstained with DAPI (blue). F, femur; T, tibia.

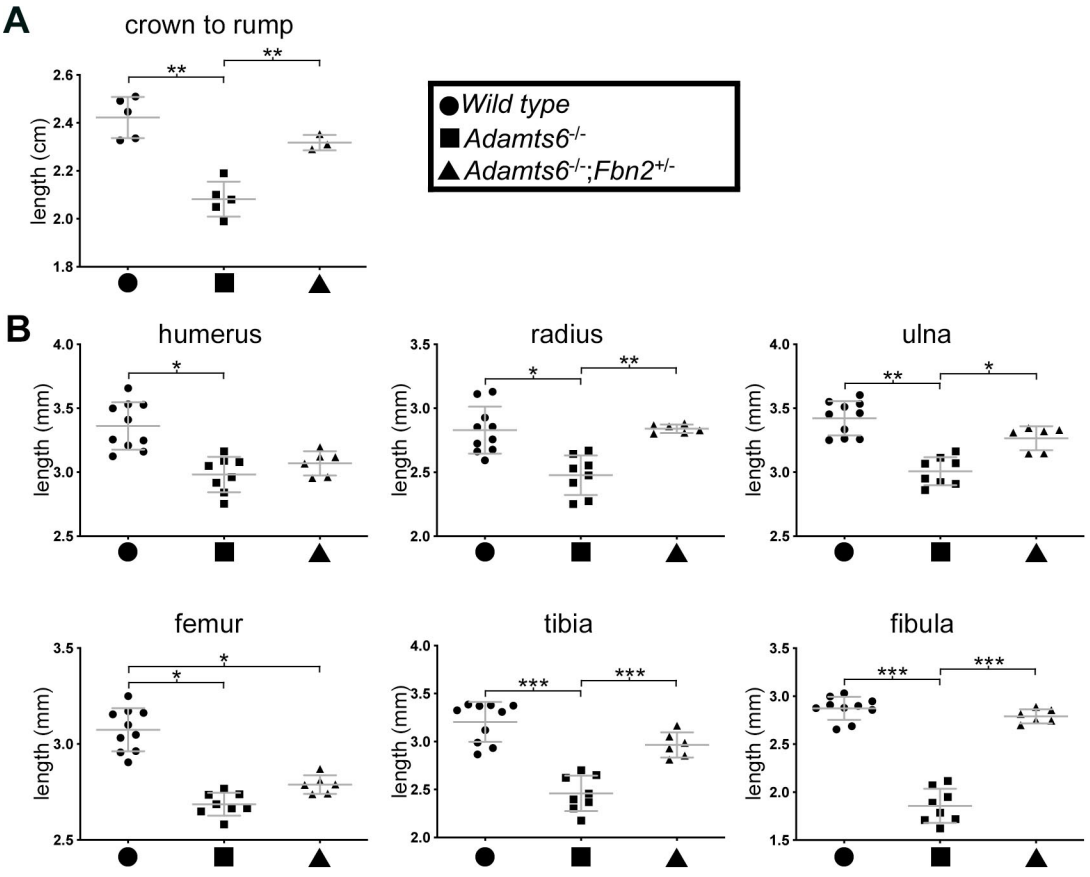

Figure 9 – figure supplement 1: Amelioration of reduced body length and long bone shortening in *Adamts6*-deficient embryos by *Fbn2* hemizygosity. Reduced crown-rump length **(A)** and reduced radius, ulna, tibia and fibula length **(B)** of *Adamts6*$^{-/-}$ E18.5 embryos is ameliorated by *Fbn2* heterozygosity. Crown-rump length, n≥ 3; bone length, n≥ 6. *≤0.05; **≤0.01; ***≤0.001.

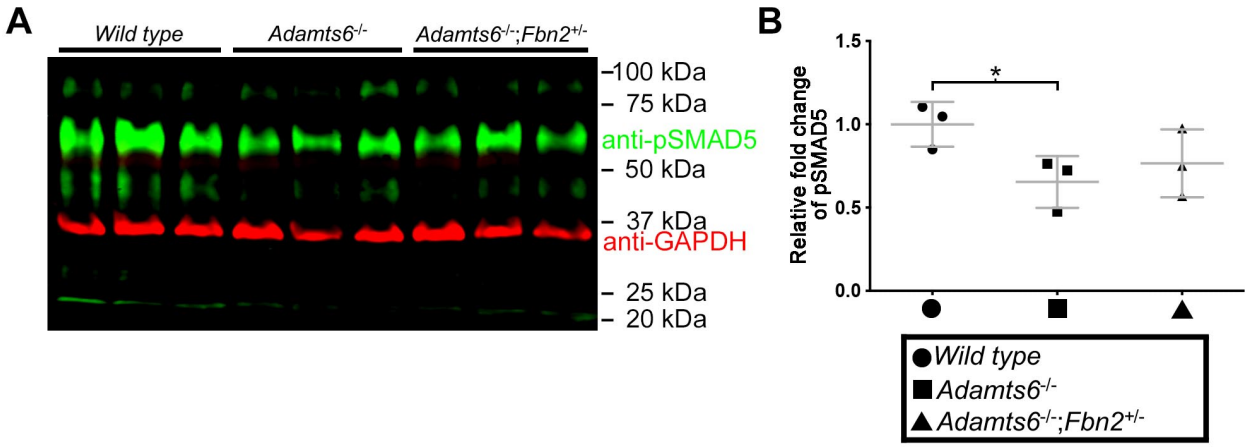

Figure 9 – figure supplement 2: BMP signaling is reduced *Adamts6*-deficient hindlimbs. **(A)** Western blot analysis show decreased anti-pSMAD5 (green; 58 kDa) content in *Adamts6*-deficient E18.5 hindlimb lysates. Anti-GAPDH (red, 37 kDa) was used as a loading control. **(B)** Normalized quantification of anti-pSMAD5 in (A) via anti-GAPDH loading control. n= 3. p*≤0.05.

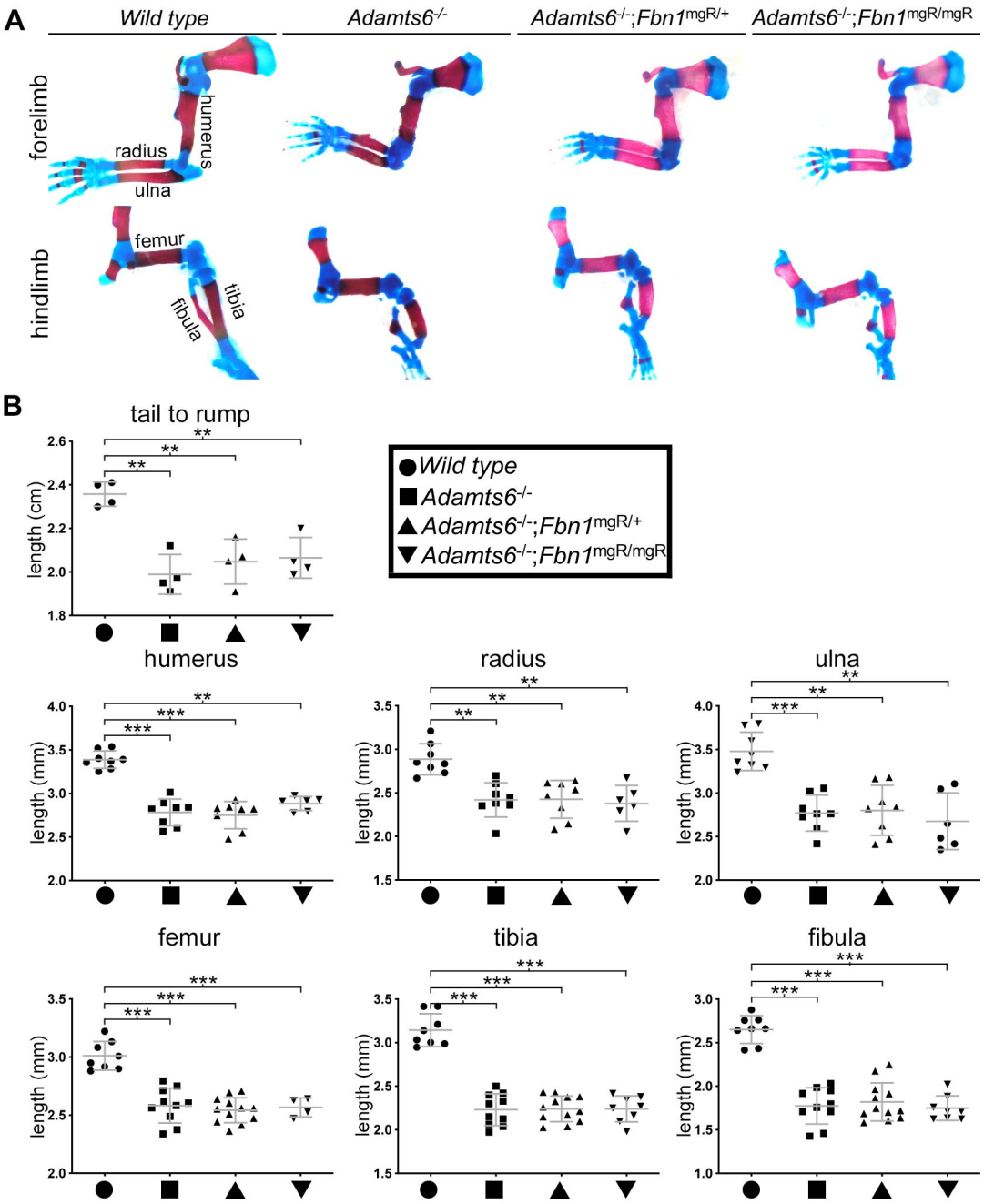

Figure 9 – figure supplement 3: No reversal in long bone shortening (A,B) or reduced crown-rump length (B) of *Adamts6*$^{-/-}$ embryos by hemizygosity or homozygosity of a *Fbn1* mutant allele, *Fbn1*^{mgR}. Measurements were made in E18.5 embryos of the indicated genotypes. Crown-rump length, n≥ 4; bone length, n≥ 4. *≤0.05; **≤0.01; ***≤0.001.

Discussion

Previously, in situ hybridization analysis demonstrated a dramatic reduction of *Fbn2* mRNA expression postnatally (Zhang et al., 1995) and corresponding to this, little fibrillin-2 was detected immunohistochemically or by proteomics in adult mouse tissues (Cain, Baldock et al., 2005, Dallas, Keene et al., 2000, De Maria et al., 2017, Hubmacher et al., 2008, Kettle, Yuan et al., 1999, Kinsey, Williamson et al., 2008). Thus, differential transcriptional regulation favors reduced fibrillin-2 synthesis postnatally, and together with dominance of *Fbn1* expression, was thought to underlie the preponderance of fibrillin-1 microfibrils in juvenile and adult mice. Prior work demonstrated that fibrillin-2 was present postnatally in only a few locations, and that some tissue microfibril bundles had a core of fibrillin-2 microfibrils surrounded by abundant fibrillin-1, suggesting that fetal microfibrils formed an inner core to which postnatal microfibrils (comprising fibrillin-1) were added (Charbonneau, Jordan et al., 2010, De Maria et al., 2017). Thus, the literature suggests that the fibrillin isoform content of microfibrils is substantially determined by the level of transcription of the respective genes. The fate of abundant fibrillin-2 microfibrils produced in the embryonic period, and the possibility of specific proteolytic mechanisms to reduce their abundance had not been previously considered.

The present work demonstrates that two homologous fibrillin-2 degrading proteases work collaboratively, but also in distinct ways, to support prevalence of fibrillin-1 in microfibrils postnatally. For example, ADAMTS10 is innately resistant to activation by furin, with only a small proportion converted to an active protease. It inconsistently cleaved fibrillin-1 and instead, promoted fibrillin-1 microfibril assembly, consistent with the observation that recessive *ADAMTS10* mutations and dominantly inherited *FBN1* mutations both led to Weill-Marchesani syndrome (Kutz et al., 2011). It was therefore thought to function akin to several ADAMTS-like proteins, which lack catalytic activity, and accelerate biogenesis of fibrillin-1 containing microfibrils (Bader, Ruhe et al., 2010, Bader, Wang et al., 2012, Gabriel, Wang et al., 2012, Hubmacher & Apte, 2015, Le Goff, Morice-Picard et al., 2008, Saito, Kurokawa et al., 2011, Tsutsui, Manabe et

al., 2010). Nevertheless, the small proportion of ADAMTS10 which was furin-activated was recently demonstrated to be proteolytically active against fibrillin-2 (Wang et al., 2019). The present work shows that like ADAMTS10, ADAMTS6, whose zymogen is efficiently activated by furin (Cain et al., 2016), cleaves fibrillin-2 in its C-terminal half. A specific ADAMTS6 cleavage site in fibrillin-2 was identified using Terminal Amine Isotopic Labeling of Substrates (TAILS), validated biochemically, and is supported by loss of fibrillin-2 microfibrils assembled by *Fbn1*$^{-/-}$ fibroblasts in the presence of active ADAMTS6. Although we are unable to purify full-length ADAMTS6 protease, and thus, cannot exclude the possibility that ADAMTS6 acts via activation of another protease in the cell culture system that was used, the direct binding of ADAMTS6 to fibrillin-2 in a binary interaction assay strongly supports the likelihood that it cleaves fibrillin-2 directly. The significance of the loss of fibrillin-2 proteolysis and its accumulation resulting from *Adamts6* inactivation was demonstrated by the dramatic reversal of the observed skeletal and palate defects after *Fbn2* haploinsufficiency in the mutant. The specificity for fibrillin-2 was further established by lack of a comparable effect after reduction of fibrillin-1.

In contrast to *Adamts6*-deficient mice, *Adamts10*$^{-/-}$ mice have subtle skeletal defects. However, persistent fibrillin-2 fibrils were noted in *Adamts10*-deficient eyes, specifically in the zonule and vitreous, as well as in skin and muscle (Mularczyk et al., 2018b, Wang et al., 2019). Together, with biochemical analysis strongly suggesting that furin-activated ADAMTS10 cleaved fibrillin-2, we concluded that ADAMTS10 was involved in proteolytic degradation of fetal fibrillin-2 microfibrils in the eye and elsewhere (Wang et al., 2019). However, despite widespread expression, it did not constitute a major activity in this regard because of its resistance to furin. The observed upregulation of *Adamts6* mRNA in *Adamts10*-deficient embryos shows it can compensate for *Adamts10* and may explain the relatively mild skeletal phenotype of *Adamts10*$^{-/-}$ mice; the markedly more severe limb anomalies in *Adamts6*$^{-/-}$;*Adamts10*$^{-/-}$ mice lead to the conclusion that both proteases have a role in fibrillin-2 turnover and may cooperate in skeletal development. While *Adamts*6 does compensate for *Adamts10*-deficiency, ADAMTS6 and

ADAMTS10 do not proteolytically activate/modify each other suggesting that they work in parallel rather than in series, using the analogy of electrical circuits.

The fate of fibrillin-2 microfibrils in adult tissue has been the subject of debate. Previous work suggested that fibrillin-2 epitope availability was reduced postnatally owing to masking by overlay of fibrillin-1. Specifically, it was shown that fibrillin-2 staining in postnatal tissues such as perichondrium was enhanced by digestion with collagenase, that microfibrils treated with chaotropic agent had enhanced reactivity to fibrillin-2 antibodies, and that *Fbn1* null juvenile mice, which die by 2 weeks of age, had robust fibrillin-2 staining (Charbonneau et al., 2010). This analysis left little doubt that fibrillin-2 fibrils do persist postnatally, but the present analysis suggests that their proteolysis by ADAMTS6, and to a lesser extent by ADAMTS10, constitutes a regulated reduction in fibrillin-2 during embryonic skeletal development. We conclude that an optimal balance between fibrillin-1 and fibrillin-2 is achieved by a dual mechanism, i.e., transcriptional regulation of both genes and ADAMTS6/10-mediated proteolysis.

The possible mechanisms by which reduced fibrillin-2 proteolysis leads to severe skeletal anomalies include dysregulated sequestration and release of growth factors of the TGFβ superfamily or mechanical constraints on limb growth caused by excess microfibrils. *Adamts6* deficiency resulted in reduced limb BMP signaling which mirrors a similar reduction of BMP signaling in *Adamts10*-mutant MEFs (Mularczyk et al., 2018b). In contrast, *Fbn2*-deficent mice have increased BMP signaling, leading to the possibility that excess fibrillin-2 microfibrils resulting from ADAMTS6/ADAMTS10 deficiency may excessively sequester BMPs (Sengle et al., 2015). Addtionally, via interaction with aggrecan, versican, fibronectin and several other ECM components, fibrillin-2 participates in several ECM networks. The observed limb phenotypes could thus reflect complex tissue effects, with altered BMP signaling being one of them.

Materials and Methods

Transgenic mice. *Adamts6*^{b2b2029Clo} (RRID: MGI:5487287), *Adamts10*^{tm1Dgen} (RRID: MGI:6355992), *Fbn1*^{mgR} and *Fbn2*^{tm1Rmz} (RRID: MGI:2445938) mice were previously described (Arteaga-Solis et al., 2001, Li, Klena et al., 2015, Pereira, Lee et al., 1999, Prins et al., 2018, Wang et al., 2019) and maintained on a C57BL/6 background. All mouse experiments were approved by the Cleveland Clinic Institutional Animal Care and Use Committee (00002450).

Histology and immunofluorescence microscopy. Mouse forelimbs and hindlimbs were fixed with 4% paraformaldehyde (PFA) in PBS at 4 ºC for 48 hrs. Sections were used for histochemistry (alcian blue staining) or for indirect immunofluorescence. The primary antibodies (Supplemental Table 1) were followed by secondary goat anti-mouse or goat anti-rabbit antibody (A11004 or A11008; 1:400; Invitrogen, Thousand Oaks, CA) treatment. Prior to immunofluorescence, citrate antigen retrieval, i.e., immersion of slides in citrate-EDTA buffer (10 mM/l citric acid, 2 mM/l EDTA, 0.05% v/v Tween-20, pH 6.2) and microwaving for 4 intervals of 1.5 min at 50% power in a microwave oven with 30 s intervals between heating cycles was utilized. In addition, hyaluronidase treatment of sections (H-2251; 0.2% in PBS; Sigma) was used prior to fibrillin-2 and fibrillin-1 immunostaining. Images were obtained using an Olympus BX51 microscope with Leica DFC 7000T camera and Leica Application Suite V4.6 software (Leica, Wetzlar, Germany). Alcian blue-stained sections used for hypertrophic chondrocyte zone length were measured along the midline of the femoral and tibial growth plate using NIH Fiji software (Schindelin, Arganda-Carreras et al., 2012) as previously reported (Mead et al., 2018b). For each embryo, data was generated from 3 separate sections, spaced at least 25 μm apart and averaged. Alizarin red-alcian blue stained skeleton preparations were performed as described (Mead, 2020). Briefly, skinned, eviscerated mice were fixed in 80% ethanol for 24 h, dehydrated in 95% ethanol for 24 h and acetone for 48 h, stained (0.1% alizarin red S, 0.3% alcian blue, 1% glacial acetic acid in

95% ethanol) for 48 h, cleared in 95% ethanol for 1 h, muscle tissue was gently removed with forceps, and the preparations were cleared in a series of increasing (20 to 80%) glycerol/1% KOH ratio until storage in 100% glycerin and photography (Leica MZ6; Insight Spot software camera and software).

RNA in situ hybridization (ISH) and β-Gal staining. Hindlimbs from *Adamts10*$^{-/-}$ embryos were fixed and β-galactosidase-stained as previously described (Mead, Du et al., 2018a), followed by paraffin embedding and 10 μm sections were obtained. *Adamts6* ISH was performed using RNAScope (Advanced Cell Diagnostics, Newark, CA) as described (Mead & Apte, 2020). Briefly, 6 μm sections were deparaffinized and hybridized to a mouse *Adamts6* probe set (428301; Advanced Cell Diagnostics) using a HybEZ™ oven (Advanced Cell Diagnostics) and the RNAScope 2.5 HD Detection Reagent Kit (322360; Advanced Cell Diagnostics) and counterstained with eosin.

Cell culture. HEK293T cells were purchased from ATCC and maintained in Dulbecco's Modified Eagles Medium (DMEM) supplemented with 10% fetal bovine serum (FBS), 100 U/ml penicillin and 100 μg/ml streptomycin at 37 °C in a 5% CO_2 humidified chamber. The cells were transiently transfected with ADAMTS6 WT or ADAMTS6 EA expression plasmids using PEI MAX (Polysciences; #24765) and were cultured with *Fbn1*$^{-/-}$ mouse embryonic fibroblasts (MEFs) in a 1:1 ratio on 8-well culture slides (Falcon; 354118). Similarily, *Adamts6*$^{-/-}$ and wild type MEFs were plated on 8-well culture slides for immunofluorescent staining. The cells were cultured for 6 days, fixed in ice-cold 70% methanol/30% acetone for 5 min at room temperature, blocked with 5% normal goat serum in PBS for 1 h at room temperature and incubated with primary antibody (see Supplemental Table 1) overnight at 4 °C as described (Hubmacher, Schneider et al., 2017). The cells were washed 3 times with PBS for 5 min at room temperature and incubated with Alexa-Fluor labeled secondary antibodies (goat anti-mouse 568 or goat anti-rabbit 488; Invitrogen A11004, A11008, respectively, 1:400).

RNA isolation and Quantitative Real-Time PCR (qRT-PCR). Mouse hindlimbs, hearts and lungs were snap-frozen and stored at -80 °C until use. Total RNA was isolated using TRIzol (15596018, Invitrogen), and 2μg of RNA was reverse transcribed into cDNA using a High-Capacity cDNA reverse transcription kit following the manufacturer's instructions (4368814; Applied Biosystems, Foster City, CA). qRT-PCR was performed with Bullseye EvaGreen qPCR MasterMix (BEQPCR-S; MIDSCI) using an Applied Biosystems 7500 instrument. The experiments were performed with three independent samples and confirmed reproducibility. *Gapdh* was used as a control for mRNA quantity. The ΔΔCt method was used to calculate relative mRNA expression levels of target genes. See Supplemental Table 2 for primer sequences.

Surface plasmon resonance analysis. The human fibrillin-2 recombinant halves (rFBN2-N and rFBN2-C, termed FBN2-Nt and FBN2-Ct in this manuscript, respectively) were purified to homogeneity (>90% purity) as described previously (Lin et al., 2002). Purified FBN2-Ct or ADAMTS6-Ct in 10 mM acetate, pH 4.0 were immobilized on a Biacore CM5 sensor chip (research grade) with the amine coupling kit following the manufacturer's instructions (GE Healthcare). 1700 resonance units of FBN2-Ct or ADAMTS6-Ct was coupled to the chip for analysis in a Biacore 3000 instrument (GE Healthcare). The kinetics analysis was performed at 25 °C in 10 mM Hepes buffer, pH 7.4 with 0.15 M NaCl, 2 mM $CaCl_2$, and 0.005% or 0.05% (v/v) surfactant P20 at a flow rate of 30 μl/min. All the analytes were diluted in the above buffer at different concentrations and injected through an uncoupled control flow cell in series with the flow cell coupled with FBN2-Ct or ADAMTS6-Ct constructs. The sample injection time was 2 min for ADAMTS6 and 3 min for FBN2 analytes. The dissociation time was 10 min. 1 M ethanolamine, pH 8.5 was used for chip surface regeneration at a flow rate of 30 μl/min for 30–60 s followed by 2 min stabilization time. All data were corrected with reference to the background binding in the control flow cell. The association and disassociation curves were generated with the

BIAevaluation software (version 4.0.1; GE Healthcare). The kinetic constants were calculated using the steady state affinity method.

Site-directed mutagenesis, transient transfection, deglycosylation and western blotting. A plasmid encoding mouse ADAMTS6 with a C-terminal myc/his tag was generated previously (Prins et al., 2018) and used for site-directed mutagenesis (Q5 Site-Directed Mutagenesis Kit; E0554; New England BioLabs) to introduce Ala at Glu^{404}, a classic metalloprotease inactivating mutation (ADAMTS6 EA). Plasmids were transfected into HEK293F cells using PEI MAX (Polysciences; #24765) and conditioned medium was collected 48-72 h later. Aliquots of medium were analyzed by 7.5% reducing SDS-PAGE. Proteins were electroblotted to polyvinylidene fluoride membranes (IPFL00010, EMD Millipore, Billerica, MA), incubated with primary antibodies (see Supplemental Table 1) overnight at 4 °C, followed by fluorescent secondary antibody goat anti mouse or rabbit (827-08365, 926-68170; 1:5000; Li-COR Biosciences, Lincoln, NE) for 1 h at room temperature. Antibody binding was visualized using an ODYSSEY CLx infrared imaging system (LI-COR). For pSMAD5 detection, hindlimbs were placed in Ripa Buffer (Abcam, ab156034) and Complete Protease Inhibitor Cocktail (Millipore, no. 4693159001) and PhosSTOP (Millipore no. 4906845001) were added prior to homogenization (T10 basic ULTRA-TURRAX (IKA, Staufen, Germany) and ultrasonication (Qsonica, Newtown, CT, USA)(3 X 2 s at 20% with 3 s pause). The supernantant was collected after centrifugation and 100 μg loaded on a 10% gel. Western blot band intensity was quantified utilizing NIH Fiji software (Schindelin et al., 2012).

TAILS sample workflow. Serum and phenol red-free conditioned medium from cell cultures were centrifuged at 4000 rcf for 20 min at 4 °C and the supernatant was filtered through a 0.22 μM filter. The medium was concentrated 20-fold using a 3 kDa (Amicon) stirring filter. Proteins were isolated using chloroform/methanol precipitation and resuspended in 2.5 M GuHCl and 250 mM HEPES pH 7.8. Protein concentration was measured using the Bradford assay (Pierce, Thermo) to determine the volume needed for 500 μg of protein from each condition. Proteins were reduced

with 10 mM dithiothreitol (DTT) for 30 min at 37 °C followed by alkylation with 20 mM N-ethylmaleimide in the dark for 20 min. The reaction was quenched by adding DTT to a final concentration of 20 mM. Proteins were labeled overnight with 40 mM light or heavy formaldehyde, which binds specifically to free N-termini and lysine residues (α and ε amines, respectively) in the presence of 20 mM sodium cyanoborohydride at 37 °C as described (Martin, Witten et al., 2020). They were treated with an additional fresh 20 mM formaldehyde and 10 mM sodium cyanoborohydride for 2 h the following day at 37 °C and the reaction was quenched with 100 mM Tris for 1 h at 37 °C. 500 μg of each channel was combined for buffer exchange on a 3 kDa molecular weight cut-off column (EMD Millipore) into 100 mM ammonium bicarbonate and digested overnight at 37 °C with mass spectrometry grade trypsin gold (Promega) at a 1:50 trypsin:protein ratio. Peptides were eluted via centrifugation and 30 μg of this digest was reserved for pre-TAILS analysis. The remaining peptides underwent enrichment using hyperbranched polyglycerol-aldehyde polymers (HPG-ALD, Flintbox, https://www.flintbox.com/public/project/1948/) at a 5:1 polymer:protein ratio. HPG-ALD binds to unblocked (i.e. trypsin-generated) amino acid termini, excluding them from the sample and enriches for blocked/labeled N-termini (Kockmann, Carte et al., 2016). The peptides were filtered through a 10 kDa MWCO column (EMD Millipore) to remove the polymer and obtain the TAILS fraction. TAILS and pre-TAILS fractions were desalted on a C18 Sep-Pak column (Waters) and eluted in 60:40 ACN: 1% trifluoroacetic acid. Samples were vacuum-centrifuged until dry and resuspended in 1% acetic acid for mass spectrometry.

Mass spectrometry. Samples were analyzed on a Thermo Ultimate 3000 UHPLC interfaced with a ThermoFisher Scientific Fusion Lumos tribrid mass spectrometer system. The HPLC column was a Dionex 15 cm x 75 μm internal diameter Acclaim Pepmap C18, 2 μm, 100 Å reversed-phase capillary chromatography column. 5 μL volumes of the extract were injected and the peptides eluted from the column by an acetonitrile/0.1% formic acid gradient at a flow rate of 0.3

µL/min were introduced into the source of the mass spectrometer on-line over a 120 min gradient. The nanospray ion source is operated at 1.9 kV. The digest was analyzed using a data-dependent method with 35% collision-induced dissociation fragmentation of the most abundant peptides every 3 s and an isolation window of 0.7 m/z for ion-trap MS/MS. Scans were conducted at a maximum resolution of 120,000 for full MS. Dynamic exclusion was enabled with a repeat count of 1 and ions within 10 ppm of the fragmented mass were excluded for 60 s.

Proteomics data analysis. Peptides were identified using a precursor mass tolerance of 10 ppm, and fragment mass tolerance of 0.6 Da. The only static modification was carbamidomethyl (C), whereas dynamic modifications included the light (28.03 Da) dimethyl formaldehyde (N-terminal, K), the heavy (34.06) dimethyl formaldehyde (N-terminal, K), oxidation (M, P), deamidation (N), acetylation (N-terminal), and Gln to pyro-Glu N-terminal cyclization. Peptides were validated using a false discovery rate (FDR) of 1% against a decoy database. Only high-confidence proteins (containing peptides at a 99% confidence level or higher) were recorded from each sample for data analysis. Pre-TAILS data required a minimum of two high-confidence peptides for protein identification and TAILS required a single peptide. Internal peptides were identified based on the criteria of having an N-terminal modification, and a sequence that does not begin prior to the third amino acid in the protein or immediately following a known signal, transit, or propeptide sequence. Peptides that met these criteria were further analyzed based on the average fold-change ratio (ADAMTS6 WT/ EA abundance) between the three technical replicate pairs. The internal peptide abundance was divided by the total protein abundance fold-change to account for differences in protein levels between groups. Peptides that met these criteria and contained a weighted ratio (ADAMTS6 WT/EA) greater than 1 underwent a t-test for significance.

Statistics. Representative data of three independent experiments are reported unless otherwise indicated. The two-tailed, unpaired Student's *t*-test was used to obtain p values. Asterisks indicate differences with statistical significance as follows: *$p \leq 0.05$; **$p \leq 0.01$; ***$p \leq 0.001$. In the dimethyl-

TAILS experiments a two-tailed, paired Student's *t*-test was used to obtain p values. Asterisks indicate differences with statistical significance as follows: *p≤0.01, #p≤0.05.

ACKNOWLEDGMENTS:

This work was supported by the Allen Distinguished Investigator Program, through support made by The Paul G. Allen Frontiers Group and the American Heart Association (to SSA), a post-doctoral fellowship from the National Institutes of Health (F32AR063548 to TJM) and the David and Lindsay Morgenthaler Postdoctoral Fellowship (to TJM). DPR was supported by the Canadian Institutes of Heatlh Research (PJT-162099) and the Marfan Foundation (USA). The Wellcome Centre for Cell-Matrix Research is supported by funding from Wellcome (203128/Z/16/Z). CB gratefully acknowledges BBSRC funding (Ref: BB/R008221/1). We thank Dr. Francesco Ramirez for *Fbn1* and *Fbn2* mutant mice.

Author contributions

TJM and SSA designed the study. TJM, LWW and DRM conducted experiments and acquired and analyzed the data. DPR, SAC and CB provided reagents and editorial assistance. TJM and SSA wrote the paper.

Table 1. Kinetic data for ADAMTS6 constructs binding to FBN2-Ct

Ligand: FBN2-Ct			
Analyte	**K_D (nM)**	**R^2**	**B_{max} (RU)**
ADAMTS6-Ct	436	0.9951	727
ADAMTS6-4TSR	122	0.8864	188
ADAMTS6-S4TSR	114	0.9819	241

Table 2. Kinetic data for FBN2 constructs binding to ADAMTS6-Ct

Ligand: ADAMTS6-Ct			
Analyte	**K_D (nM)**	**R^2**	**B_{max} (RU)**
FBN2-Nt	43	0.9972	85
FBN2-Ct	80	0.9933	100

Supplemental Table 1. Antibodies

Name	**Product info**	**dilution**
anti-Fibrillin-2-gly	(Trask, Trask et al., 2000)	IF: 1:300
anti-mFbn1-C	(Shi, Jones et al., 2020)	IF: 1:500
anti-Col X	Abcam ab58632	IF: 1:1000
anti-rFBN2-C	(Lin et al., 2002)	WB: 1:500
Anti-His	R&D MAB050	IF: 1:400 WB: 1:1000
Anti-pSMAD5	Abcam ab92698	WB: 1:1000
Anti-GAPDH	EMD Millipore MAB374	WB: 1:5000

Supplemental Table 2. Quantitative Real-Time PCR primers

Adamts6	Forward: 5´-TCTCTAGCTCATAGGTAGCCC-3´
	Reverse: 5´-GTTTAGGTGAAAGTGCTTGCC-3´
Adamts10	Forward: 5´-CATCACACGCTATGACATCTG-3´
	Reverse: 5´-CACGAATGGATTAGTCTTCATGG-3´
Fbn2	Forward: 5´-AACGATTGCCTAGACATAGAC-3´
	Reverse: 5´-TTCGCTTCTCACTTCATATCC-3´
Fbn1	Forward: 5´-GCTGTGAATGCGACATGGGCTT-3´
	Reverse: 5´-TCTCACACTCGCAACGGAAGAG-3´
Gapdh	Forward: 5´-TGGAGAAACCTGCCAAGTATGA-3´
	Reverse: 5´-CTGTTGAAGTCGCAGGAGACA-3´

REFERENCES

Arteaga-Solis E, Gayraud B, Lee SY, Shum L, Sakai L, Ramirez F (2001) Regulation of limb patterning by extracellular microfibrils. *J Cell Biol* 154: 275-81

Bader HL, Ruhe AL, Wang LW, Wong AK, Walsh KF, Packer RA, Mitelman J, Robertson KR, O'Brien DP, Broman KW, Shelton GD, Apte SS, Neff MW (2010) An ADAMTSL2 founder mutation causes Musladin-Lueke Syndrome, a heritable disorder of beagle dogs, featuring stiff skin and joint contractures. *PLoS One* 5: e12817

Bader HL, Wang LW, Ho JC, Tran T, Holden P, Fitzgerald J, Atit RP, Reinhardt DP, Apte SS (2012) A disintegrin-like and metalloprotease domain containing thrombospondin type 1 motif-like 5 (ADAMTSL5) is a novel fibrillin-1-, fibrillin-2-, and heparin-binding member of the ADAMTS superfamily containing a netrin-like module. *Matrix Biol* 31: 398-411

Bekhouche M, Leduc C, Dupont L, Janssen L, Delolme F, Vadon-Le Goff S, Smargiasso N, Baiwir D, Mazzucchelli G, Zanella-Cleon I, Dubail J, De Pauw E, Nusgens B, Hulmes DJ, Moali C, Colige A (2016) Determination of the substrate repertoire of ADAMTS2, 3, and 14 significantly broadens their functions and identifies extracellular matrix organization and TGF-beta signaling as primary targets. *FASEB J* 30: 1741-56

Cain SA, Baldock C, Gallagher J, Morgan A, Bax DV, Weiss AS, Shuttleworth CA, Kielty CM (2005) Fibrillin-1 interactions with heparin. Implications for microfibril and elastic fiber assembly. *J Biol Chem* 280: 30526-37

Cain SA, Morgan A, Sherratt MJ, Ball SG, Shuttleworth CA, Kielty CM (2006) Proteomic analysis of fibrillin-rich microfibrils. *Proteomics* 6: 111-22

Cain SA, Mularczyk EJ, Singh M, Massam-Wu T, Kielty CM (2016) ADAMTS-10 and -6 differentially regulate cell-cell junctions and focal adhesions. *Sci Rep* 6: 35956

Charbonneau NL, Dzamba BJ, Ono RN, Keene DR, Corson GM, Reinhardt DP, Sakai LY (2003) Fibrillins can co-assemble in fibrils, but fibrillin fibril composition displays cell-specific differences. *J Biol Chem* 278: 2740-9

Charbonneau NL, Jordan CD, Keene DR, Lee-Arteaga S, Dietz HC, Rifkin DB, Ramirez F, Sakai LY (2010) Microfibril structure masks fibrillin-2 in postnatal tissues. *J Biol Chem* 285: 20242-51

Corson GM, Charbonneau NL, Keene DR, Sakai LY (2004) Differential expression of fibrillin-3 adds to microfibril variety in human and avian, but not rodent, connective tissues. *Genomics* 83: 461-72

Dagoneau N, Benoist-Lasselin C, Huber C, Faivre L, Megarbane A, Alswaid A, Dollfus H, Alembik Y, Munnich A, Legeai-Mallet L, Cormier-Daire V (2004) ADAMTS10 mutations in autosomal recessive Weill-Marchesani syndrome. *Am J Hum Genet* 75: 801-6

Dallas SL, Keene DR, Bruder SP, Saharinen J, Sakai LY, Mundy GR, Bonewald LF (2000) Role of the latent transforming growth factor beta binding protein 1 in fibrillin-containing microfibrils in bone cells in vitro and in vivo. *J Bone Miner Res* 15: 68-81

De Maria A, Wilmarth PA, David LL, Bassnett S (2017) Proteomic Analysis of the Bovine and Human Ciliary Zonule. *Invest Ophthalmol Vis Sci* 58: 573-585

Dubail J, Apte SS (2015) Insights on ADAMTS proteases and ADAMTS-like proteins from mammalian genetics. *Matrix Biol* 44-46: 24-37

Dubail J, Aramaki-Hattori N, Bader HL, Nelson CM, Katebi N, Matuska B, Olsen BR, Apte SS (2014) A new Adamts9 conditional mouse allele identifies its non-redundant role in interdigital web regression. *Genesis* 52: 702-12

Enomoto H, Nelson, C., Somerville, R.P.T., Mielke, K., Dixon, L., Powell, K., Apte, S.S. (2010) Cooperation of two ADAMTS metalloproteases in closure of the mouse palate identifies a requirement for versican proteolysis in regulating palatal mesenchyme proliferation. *Development* 137: 4029-4038

Faivre L, Gorlin RJ, Wirtz MK, Godfrey M, Dagoneau N, Samples JR, Le Merrer M, Collod-Beroud G, Boileau C, Munnich A, Cormier-Daire V (2003) In frame fibrillin-1 gene deletion in autosomal dominant Weill-Marchesani syndrome. *J Med Genet* 40: 34-6

Fujikawa Y, Yoshida H, Inoue T, Ohbayashi T, Noda K, von Melchner H, Iwasaka T, Shiojima I, Akama TO, Nakamura T (2017) Latent TGF-β binding protein 2 and 4 have essential overlapping functions in microfibril development. *Sci Rep* 7: 43714

Gabriel LA, Wang LW, Bader H, Ho JC, Majors AK, Hollyfield JG, Traboulsi EI, Apte SS (2012) ADAMTSL4, a secreted glycoprotein widely distributed in the eye, binds fibrillin-1 microfibrils and accelerates microfibril biogenesis. *Invest Ophthalmol Vis Sci* 53: 461-469

Hubmacher D, Apte SS (2015) ADAMTS proteins as modulators of microfibril formation and function. *Matrix Biol* 47: 34-43

Hubmacher D, El-Hallous EI, Nelea V, Kaartinen MT, Lee ER, Reinhardt DP (2008) Biogenesis of extracellular microfibrils: Multimerization of the fibrillin-1 C terminus into bead-like structures enables self-assembly. *Proc Natl Acad Sci U S A* 105: 6548-53

Hubmacher D, Schneider M, Berardinelli SJ, Takeuchi H, Willard B, Reinhardt DP, Haltiwanger RS, Apte SS (2017) Unusual life cycle and impact on microfibril assembly of ADAMTS17, a secreted metalloprotease mutated in genetic eye disease. *Sci Rep* 7: 41871

Huxley-Jones J, Apte SS, Robertson DL, Boot-Handford RP (2005) The characterisation of six ADAMTS proteases in the basal chordate Ciona intestinalis provides new insights into the vertebrate ADAMTS family. *Int J Biochem Cell Biol* 37: 1838-45

Huxley-Jones J, Clarke TK, Beck C, Toubaris G, Robertson DL, Boot-Handford RP (2007) The evolution of the vertebrate metzincins; insights from Ciona intestinalis and Danio rerio. *BMC Evol Biol* 7: 63

Huxley-Jones J, Robertson DL, Boot-Handford RP (2007) On the origins of the extracellular matrix in vertebrates. *Matrix Biol* 26: 2-11

Karoulias SZ, Taye N, Stanley S, Hubmacher D (2020) The ADAMTS/Fibrillin Connection: Insights into the Biological Functions of ADAMTS10 and ADAMTS17 and Their Respective Sister Proteases. *Biomolecules* 10

Kettle S, Yuan X, Grundy G, Knott V, Downing AK, Handford PA (1999) Defective calcium binding to fibrillin-1: consequence of an N2144S change for fibrillin-1 structure and function. *J Mol Biol* 285: 1277-87

Kinsey R, Williamson MR, Chaudhry S, Mellody KT, McGovern A, Takahashi S, Shuttleworth CA, Kielty CM (2008) Fibrillin-1 microfibril deposition is dependent on fibronectin assembly. *J Cell Sci* 121: 2696-704

Kleifeld O, Doucet A, auf dem Keller U, Prudova A, Schilling O, Kainthan RK, Starr AE, Foster LJ, Kizhakkedathu JN, Overall CM (2010) Isotopic labeling of terminal amines in complex samples identifies protein N-termini and protease cleavage products. *Nat Biotechnol* 28: 281-8

Kockmann T, Carte N, Melkko S, auf dem Keller U (2016) Identification of Protease Substrates in Complex Proteomes by iTRAQ-TAILS on a Thermo Q Exactive Instrument. In *Analysis of Post-Translational Modifications and Proteolysis in Neuroscience*, Grant JE, Li H (eds) pp 187-207. New York, NY: Springer New York

Kockmann T, Carte, N., Melkko, S. & Keller, U.a.d. (2016) Identification of Protease Substrates in Complex Proteomes by iTRAQ-TAILs on a Thermo Q Exactive Instrument In *Neuromethods* Grant JE, Li, H. (ed) pp 187–207. New York: Springer Science+Business Media

Kozel BA, Mecham RP (2019) Elastic fiber ultrastructure and assembly. *Matrix Biol* 84: 31-40

Kutz WE, Wang LW, Bader HL, Majors AK, Iwata K, Traboulsi EI, Sakai LY, Keene DR, Apte SS (2011) ADAMTS10 Protein Interacts with Fibrillin-1 and Promotes Its Deposition in Extracellular Matrix of Cultured Fibroblasts. *J Biol Chem* 286: 17156-67

Le Goff C, Morice-Picard F, Dagoneau N, Wang LW, Perrot C, Crow YJ, Bauer F, Flori E, Prost-Squarcioni C, Krakow D, Ge G, Greenspan DS, Bonnet D, Le Merrer M, Munnich A, Apte SS,

Cormier-Daire V (2008) ADAMTSL2 mutations in geleophysic dysplasia demonstrate a role for ADAMTS-like proteins in TGF-beta bioavailability regulation. *Nat Genet* 40: 1119-23

Li Y, Klena NT, Gabriel GC, Liu X, Kim AJ, Lemke K, Chen Y, Chatterjee B, Devine W, Damerla RR, Chang C, Yagi H, San Agustin JT, Thahir M, Anderton S, Lawhead C, Vescovi A, Pratt H, Morgan J, Haynes L et al. (2015) Global genetic analysis in mice unveils central role for cilia in congenital heart disease. *Nature* 521: 520-4

Lin G, Tiedemann K, Vollbrandt T, Peters H, Batge B, Brinckmann J, Reinhardt DP (2002) Homo- and heterotypic fibrillin-1 and -2 interactions constitute the basis for the assembly of microfibrils. *J Biol Chem* 277: 50795-804

Marson A, Rock MJ, Cain SA, Freeman LJ, Morgan A, Mellody K, Shuttleworth CA, Baldock C, Kielty CM (2005) Homotypic fibrillin-1 interactions in microfibril assembly. *J Biol Chem* 280: 5013-21

Martin DR, Witten JC, Tan CD, Rodriguez ER, Blackstone EH, Pettersson GB, Seifert DE, Willard BB, Apte SS (2020) Proteomics identifies a convergent innate response to infective endocarditis and extensive proteolysis in vegetation components. *JCI Insight* 5

McCulloch DR, Nelson CM, Dixon LJ, Silver DL, Wylie JD, Lindner V, Sasaki T, Cooley MA, Argraves WS, Apte SS (2009) ADAMTS metalloproteases generate active versican fragments that regulate interdigital web regression. *Dev Cell* 17: 687-98

Mead TJ (2020) Alizarin Red and Alcian Blue Preparations to Visualize the Skeleton. *Methods Mol Biol* 2043: 207-212

Mead TJ, Apte SS (2018) ADAMTS proteins in human disorders. *Matrix Biol* 71-72: 225-239

Mead TJ, Apte SS (2020) Expression Analysis by RNAscope In Situ Hybridization. *Methods Mol Biol* 2043: 173-178

Mead TJ, Du Y, Nelson CM, Gueye NA, Drazba J, Dancevic CM, Vankemmelbeke M, Buttle DJ, Apte SS (2018a) ADAMTS9-Regulated Pericellular Matrix Dynamics Governs Focal Adhesion-Dependent Smooth Muscle Differentiation. *Cell Rep* 23: 485-498

Mead TJ, McCulloch DR, Ho JC, Du Y, Adams SM, Birk DE, Apte SS (2018b) The metalloproteinase-proteoglycans ADAMTS7 and ADAMTS12 provide an innate, tendon-specific protective mechanism against heterotopic ossification. *JCI Insight* 3

Mecham RP, Gibson MA (2015) The microfibril-associated glycoproteins (MAGPs) and the microfibrillar niche. *Matrix Biol* 47: 13-33

Mularczyk EJ, Singh M, Godwin ARF, Galli F, Humphreys N, Adamson AD, Mironov A, Cain SA, Sengle G, Boot-Handford RP, Cossu G, Kielty CM, Baldock C (2018a) ADAMTS10-mediated tissue disruption in Weill-Marchesani Syndrome. *Hum Mol Genet*

Mularczyk EJ, Singh M, Godwin ARF, Galli F, Humphreys N, Adamson AD, Mironov A, Cain SA, Sengle G, Boot-Handford RP, Cossu G, Kielty CM, Baldock C (2018b) ADAMTS10-mediated tissue disruption in Weill-Marchesani syndrome. *Hum Mol Genet* 27: 3675-3687

Nandadasa S, Kraft CM, Wang LW, O'Donnell A, Patel R, Gee HY, Grobe K, Cox TC, Hildebrandt F, Apte SS (2019) Secreted metalloproteases ADAMTS9 and ADAMTS20 have a non-canonical role in ciliary vesicle growth during ciliogenesis. *Nat Commun* 10: 953

Nandadasa S, Nelson CM, Apte SS (2015) ADAMTS9-Mediated Extracellular Matrix Dynamics Regulates Umbilical Cord Vascular Smooth Muscle Differentiation and Rotation. *Cell Rep* 11: 1519-28

Nistala H, Lee-Arteaga S, Smaldone S, Siciliano G, Carta L, Ono RN, Sengle G, Arteaga-Solis E, Levasseur R, Ducy P, Sakai LY, Karsenty G, Ramirez F (2010) Fibrillin-1 and -2 differentially modulate endogenous TGF-beta and BMP bioavailability during bone formation. *J Cell Biol* 190: 1107-21

Pereira L, Lee SY, Gayraud B, Andrikopoulos K, Shapiro SD, Bunton T, Biery NJ, Dietz HC, Sakai LY, Ramirez F (1999) Pathogenetic sequence for aneurysm revealed in mice underexpressing fibrillin-1. *Proc Natl Acad Sci U S A* 96: 3819-23

Prins BP, Mead TJ, Brody JA, Sveinbjornsson G, Ntalla I, Bihlmeyer NA, van den Berg M, Bork-Jensen J, Cappellani S, Van Duijvenboden S, Klena NT, Gabriel GC, Liu X, Gulec C, Grarup N, Haessler J, Hall LM, Iorio A, Isaacs A, Li-Gao R et al. (2018) Exome-chip meta-analysis identifies novel loci associated with cardiac conduction, including ADAMTS6. *Genome Biol* 19: 87

Ramirez F, Caescu C, Wondimu E, Galatioto J (2018) Marfan syndrome; A connective tissue disease at the crossroads of mechanotransduction, TGFβ signaling and cell stemness. *Matrix Biol* 71-72: 82-89

Ricard-Blum S, Vallet SD (2019) Fragments generated upon extracellular matrix remodeling: Biological regulators and potential drugs. *Matrix Biol* 75-76: 170-189

Robinson PN, Arteaga-Solis E, Baldock C, Collod-Beroud G, Booms P, De Paepe A, Dietz HC, Guo G, Handford PA, Judge DP, Kielty CM, Loeys B, Milewicz DM, Ney A, Ramirez F, Reinhardt DP, Tiedemann K, Whiteman P, Godfrey M (2006) The molecular genetics of Marfan syndrome and related disorders. *J Med Genet* 43: 769-87

Sabatier L, Miosge N, Hubmacher D, Lin G, Davis EC, Reinhardt DP (2011) Fibrillin-3 expression in human development. *Matrix Biol* 30: 43-52

Saito M, Kurokawa M, Oda M, Oshima M, Tsutsui K, Kosaka K, Nakao K, Ogawa M, Manabe R, Suda N, Ganjargal G, Hada Y, Noguchi T, Teranaka T, Sekiguchi K, Yoneda T, Tsuji T (2011) ADAMTSL6beta protein rescues fibrillin-1 microfibril disorder in a Marfan syndrome mouse model through the promotion of fibrillin-1 assembly. *J Biol Chem* 286: 38602-13

Schindelin J, Arganda-Carreras I, Frise E, Kaynig V, Longair M, Pietzsch T, Preibisch S, Rueden C, Saalfeld S, Schmid B, Tinevez JY, White DJ, Hartenstein V, Eliceiri K, Tomancak P, Cardona A (2012) Fiji: an open-source platform for biological-image analysis. *Nat Methods* 9: 676-82

Sengle G, Carlberg V, Tufa SF, Charbonneau NL, Smaldone S, Carlson EJ, Ramirez F, Keene DR, Sakai LY (2015) Abnormal Activation of BMP Signaling Causes Myopathy in Fbn2 Null Mice. *PLoS Genet* 11: e1005340

Shi Y, Jones W, Beatty W, Tan Q, Mecham RP, Kumra H, Reinhardt DP, Gibson MA, Reilly MA, Rodriguez J, Bassnett S (2020) Latent-transforming growth factor beta-binding protein-2 (LTBP-2) is required for longevity but not for development of zonular fibers. *Matrix Biol*

Shin SJ, Yanagisawa H (2019) Recent updates on the molecular network of elastic fiber formation. *Essays Biochem* 63: 365-376

Somerville RP, Jungers KA, Apte SS (2004) ADAMTS10: Discovery and characterization of a novel, widely expressed metalloprotease and its proteolytic activation. *J Biol Chem* 279: 51208-17

Thomson J, Singh M, Eckersley A, Cain SA, Sherratt MJ, Baldock C (2019) Fibrillin microfibrils and elastic fibre proteins: Functional interactions and extracellular regulation of growth factors. *Semin Cell Dev Biol* 89: 109-117

Trask TM, Trask BC, Ritty TM, Abrams WR, Rosenbloom J, Mecham RP (2000) Interaction of tropoelastin with the amino-terminal domains of fibrillin-1 and fibrillin-2 suggests a role for the fibrillins in elastic fiber assembly. *J Biol Chem* 275: 24400-6

Tsutsui K, Manabe RI, Yamada T, Nakano I, Oguri Y, Keene DR, Sengle G, Sakai LY, Sekiguchi K (2010) A disintegrin and metalloproteinase with thrombospondin motifs-like-6 (ADAMTSL-6) is a novel extracellular matrix protein that binds to fibrillin-1 and promotes fibrillin-1 fibril formation. *J Biol Chem* 285: 4870-82

Wang LW, Kutz WE, Mead TJ, Beene LC, Singh S, Jenkins MW, Reinhardt DP, Apte SS (2019) Adamts10 inactivation in mice leads to persistence of ocular microfibrils subsequent to reduced fibrillin-2 cleavage. *Matrix Biol* 77: 117-128

Yip RKH, Chan D, Cheah KSE (2019) Mechanistic insights into skeletal development gained from genetic disorders. *Curr Top Dev Biol* 133: 343-385

Zhang H, Apfelroth SD, Hu W, Davis EC, Sanguineti C, Bonadio J, Mecham RP, Ramirez F (1994) Structure and expression of fibrillin-2, a novel microfibrillar component preferentially located in elastic matrices. *J Cell Biol* 124: 855-63

Zhang H, Hu W, Ramirez F (1995) Developmental expression of fibrillin genes suggests heterogeneity of extracellular microfibrils. *J Cell Biol* 129: 1165-76